Current Research in Food Science 5 (2022) 1625–1639

Contents lists available at ScienceDirect

Current Research in Food Science

journal homepage: www.sciencedirect.com/journal/current-research-in-food-science

Development of fish gelatin-chitooligosaccharide conjugates through the Maillard reaction for the encapsulation of curcumin

Sheng Lin, Xixi Cai, Huimin Chen, Yizhou Xu, Jiulin Wu **, Shaoyun Wang *

College of Biological Science and Engineering, Fuzhou University, Fuzhou, 350108, PR China

ARTICLE INFO

Editor name; Dr. Xing Chen

Keywords:
Fish gelatin
Chitooligosaccharide
Maillard reaction
Curcumin
Enhanced antioxidant capacity

ABSTRACT

The poor water solubility, bioavailability and stability of bioactive compounds have become the bottleneck restricting their wide application, thus developing a functional carrier to realize the efficient encapsulation and activity improvement of active hydrophobic substances has become a research hotspot. In this work, a functional glycosylated fish gelatin (called FG-COS conjugates) carrier based on fish gelatin (FG) and chitooligosaccharide (COS) via Maillard reaction was developed. The functional carrier exhibited good antioxidant activity and high encapsulation of curcumin (Cur). Enhanced antioxidant effect of Cur loaded in FG-COS conjugates (called FG–COS–Cur nanoparticles) was achieved, showing remarkable UV protection on Cur and enhanced intracellular antioxidant activity of FG–COS–Cur nanoparticles. Remarkably, FG–COS–Cur nanoparticles increased the cell viability of H_2O_2-induced oxidative damage Caco-2 cells, drastically reduced the levels of reactive oxygen species (ROS) and lactate dehydrogenase (LDH), and significantly increased intracellular antioxidant enzyme activities, which all exhibited a dose-response relationship. These findings suggested that the FG-COS conjugates with intrinsic antioxidant activity could effectively encapsulate Cur and improved bioavailability for hydrophobic active molecules in functional food field.

1. Introduction

Many bioactive components are used in food as functional ingredients. However, a good number of bioactive compounds have poor water solubility and bioavailability, and are easily degraded. In order to improve their stability and bioavailability, numerous carriers are developed (Bao et al., 2019). The covalent complexes formed by Maillard reaction are one of the effective carriers (Wang et al., 2021). These reactions do not require the addition of chemical reagents, instead, proceed spontaneously only by simple heating to obtain Maillard reaction products (MRPs). The glycoconjugates formed during the reaction significantly improve the emulsification performance, foaming properties, antioxidant capacity and stability of proteins, so glycoconjugates are also suitable for use as an encapsulation carrier (Jia et al., 2020; Sheng et al., 2020; Zhong et al., 2019).

Fish gelatin (FG) is mostly obtained from fish products waste such as fish skin, bones, scales, and gills (Hu et al., 2021). It is considered to be the ideal and most potential substitute for mammalian gelatin (Lv et al., 2019). Nevertheless, due to inferior surface-active properties and poor antioxidant, using natural active substances to modify gelatin has been considered to improve these performance (Huang et al., 2020). Chitosan is a polysaccharide made up of glucosamine and N-acetyl glucosamine, but the application of chitosan is limited by its poor water solubility (Yu et al., 2019). Compared with chitosan, chitooligosaccharide (COS) has better water solubility, biocompatibility and owns a wide range of biological functions, such as antioxidant activity, anti-inflammatory, immunomodulation (Cao et al., 2018; Yuan et al., 2019) and so on. However, there are few reports on modification of FG by COS glycosylation.

Curcumin (Cur) is a natural polyphenol compound that can be extracted easily from turmeric (Li et al., 2021). It has been reported to possess antioxidant (Fan et al., 2018), antibacterial (Zhang et al., 2021b), antitumor (Jordan et al., 2016), anti-inflammatory (Bernardo et al., 2021), which have great development prospects. However, its shortcomings such as low water solubility and low bioavailability have always severely limit its wide application (Rauf et al., 2018). To solve these problems, researchers create Cur delivery nanocarriers, such as biomacromolecule particles (Wu et al., 2017) liposomes (Cheng et al.,

* Corresponding author. College of Biological Science and Engineering, Fuzhou University, Fuzhou, 350108, China.
** Corresponding author. College of Biological Science and Engineering, Fuzhou University, Fuzhou, 350108, China.
E-mail addresses: wujiul590@126.com (J. Wu), shywang@fzu.edu.cn (S. Wang).

https://doi.org/10.1016/j.crfs.2022.09.019
Received 14 July 2022; Received in revised form 30 August 2022; Accepted 16 September 2022
Available online 17 September 2022

2017) and emulsions (Jiang et al., 2020). These new delivery strategies can be used to enhance the bioavailability of Cur and have broad application prospect in the field of functional foods.

Hence, the purpose of this study was to fabricate functional carriers for efficient encapsulation of Cur with enhanced antioxidant activity. Firstly, we used FG and COS to prepare functional carrier (FG-COS conjugates) through Maillard reaction, then optimized the preparation process. Micromorphology, FTIR and XRD, emulsification, surface hydrophobicity and antioxidant activity of FG-COS conjugates were characterized. Simultaneously, we fabricated FG–COS–Cur nanoparticles based on FG-COS conjugates high hydrophobicity, then the encapsulation efficiency, stability, antioxidant activity, cellular uptake and oxidation resistance on Caco-2 cells were also be characterized.

2. Materials and methods

2.1. Materials

Fish gelatin (FG), 2,2-diphenyl-1-picrylhydrazyl (DPPH) were purchased from Sigma-Aldrich Chemical Inc. (St Louis, MO, USA). Chitooligosaccharide (COS) was obtained from Hai De Bei Marine Biological Engineering Co., Ltd. (Shandong, China). Curcumin (Cur), 8-aniline-1-naphthalenesulfonic acid (ANS), urea, tris, glycine, ethylene diamine tetraacetic acid (EDTA), 5,5′-Dithiobis (DTNB), 3-(4,5)-dimethylthiahiazo (-z-y1)-3,5-di-phenytetrazoliumromide (MTT) were purchased from Shanghai Yuanye Bio-Technology Co., Ltd. (Shanghai, China). $K_3(Fe(CN)_6)$, Trichloroacetic acid (TCA) and $FeCl_3$ were obtained from Aladdin Industrial Co., Ltd. (Shanghai, China). Sodium dodecyl sulfate (SDS), anhydrous ethanol and hydrogen peroxide were bought from Xilong Scientific Co., Ltd. (Shantou, China). Caco-2 cells were obtained from BeNa Culture Collection (Kunshan, China). Dimethyl sulfoxide (DMSO) was purchased from Sinopharm Chemical Reagent Co., Ltd. (Shanghai, China). Reactive oxygen species (ROS) assay kit was purchased from Biyuntian Biotechnology Co., Ltd. (Shanghai, China), lactate dehydrogenase (LDH), Superoxide dismutase (SOD), Catalase (CAT) and protein content assay kit was purchased from Jiancheng Institute of Biological Engineering Co., Ltd. (Nanjing, China).

2.2. Preparation of fish gelatin-chitooligosaccharide conjugates (FG-COS conjugates)

The DPPH radical scavenging rate, $A_{294\ nm}$ and $A_{420\ nm}$ were used as indicators to explore the effect of reaction times (1, 2, 3, 4, 5, 6 h), reaction temperatures (70, 80, 90, 100 °C), different glycoprotein ratios (1:3, 1:2, 1:1, 2:1, 3:1), different total concentrations (30, 50, 70, 90 mg/mL) and different initial pH (4, 5, 6, 7, 8) on FG/COS Maillard reaction.

Each sample obtained by Maillard reaction was diluted to 5 mg/mL, corresponding to the UV spectrophotometer to detect and calculate the value of $A_{294\ nm}$, $A_{420\ nm}$ and DPPH radical scavenging rate.

According to the above-mentioned optimal conditions, the final conditions of the Maillard reaction were determined and the preparation of FG-COS conjugates was carried out. The obtained FG-COS conjugates were cooled, freeze-dried, stored at −20 °C and could be dispersed and dissolved in water by stirring at room temperature.

2.2.1. The monitoring of FG/COS Maillard reaction products

During the Maillard reaction, intermediate active products such as ketones and aldehydes were produced. These substances had ultraviolet absorption at a wavelength of 294 nm. Therefore, the level of $A_{294\ nm}$ indicated that many of intermediate products generated in the Maillard reaction. And the degree of browning of the Maillard process and the degree of production of the end products were determined by the absorbance at 420 nm (Ajandouz et al., 2001). The values of $A_{294\ nm}$ and $A_{420\ nm}$ measured by UV spectrophotometer (Genesys 10s, Thermo Fisher Scientific Inc) could monitor the Maillard reaction degree of FG and COS under different reaction conditions.

2.2.2. DPPH radical scavenging rate of FG/COS Maillard reaction products

DPPH radical scavenging rate was referred to Dai et al. (2017) with slight modifications. In short, 0.1 mM DPPH solution was prepared with absolute ethanol in the dark. 1 mL of the sample solution and an equal volume of DPPH solution were mixing thoroughly, and the solution was placed for 30 min in an environment without light. The absorbance of the sample solution was then measured using a UV–visible spectrometer at 517 nm. The DPPH radical scavenging rate was calculated using the following equation:

$$\text{DPPH radical scavenging rate } (\%) = [1\text{-}(A_i\text{-}A_j)/A_0] \times 100\% \quad (1)$$

where A_0 represented the absorbance of the blank group, A_i represented the absorbance of the sample group, and Aj represented the absorbance of the reference group.

2.3. Characterization of FG-COS conjugates

2.3.1. Atomic force microscopy (AFM)

The surface morphology of FG-COS conjugates was investigated using an AFM (5500AFM, Agilent Instrument Inc). With deionized water, the FG-COS conjugates was diluted to 0.1 mg/mL, and 2 μL was taken and applied onto the freshly peeled mica sheet's surface. Before testing, all of the samples were allowed to dry at room temperature overnight. Images were scanned in tapping mode. The Digital Nanoscope program was used to examine and calculate the collected spectra.

2.3.2. Scanning electron microscope (SEM)

The FG-COS conjugates was diluted to 0.1 mg/mL with deionized water, and 2 μL of the diluted sample was dropped onto the alcohol-washed silicon wafer and air-dried overnight. The microscopic morphology of the FG-COS conjugates were observed with a dual-beam field emission SEM (Nova NanoSEM 230, Czech Republic Inc).

2.3.3. Fourier transform infrared spectroscopy analysis

The powders of FG, COS, and FG-COS conjugates were combined with potassium bromide and grounded into a homogeneous powder using an agate mortar. Then samples were surveyed on a FTIR spectrometer (Avatar 360, Thermo Nicolet Inc). The scanning range applied was 400–4000 cm^{-1} with 64 scans at 4 cm^{-1} resolution.

2.3.4. X-ray diffraction analysis

FG, COS, and FG-COS conjugates powder were added to a flat XRD glass slide using molds to make a rectangle, and then placed on the operation board for X-ray diffractometer (Xpert3, CEM Inc) testing. The operating conditions were 40 kV and 40 mA, and all samples were recorded in the scattering angle range from 3° to 90°.

2.3.5. Emulsification performance of FG/FG-COS conjugates

PBS buffer (0.2 M, pH 7.0) was used to dilute the FG and FG-COS conjugates to 10 mg/mL. 3 mL soybean oil and 9 mL sample solution were put into a centrifuge tube. After high-speed homogenization at 12000 rpm for 60 s, 50 μL emulsion from the bottom of the centrifuge tube was sucked at 0 and 10 min and mixed with 5 mL SDS (1 mg/mL). The solution was quickly shaken and mixed with a vortex oscillator (MX-S Mixers, Scilogex), and then the absorbance value was measured at 500 nm with an UV spectrophotometer, which was recorded as A_0 and A_{10}, respectively. The following formulas were used to determine the emulsification activity index (EAI) and emulsification stability index (ESI):

$$\text{EAI } (m^2/g) = 2TA_0 \times \text{dilution factor}/10000c\varphi L \quad (2)$$

$$\text{ESI (min)} = 10A_0/A_0\text{-}A_{10} \quad (3)$$

In the formula, T was the constant 2.303, the dilution factor was 100, c was the sample concentration (g/mL), φ was the oil volumetric fraction (0.25), and L was 1.

2.3.6. Foaming performance of FG/FG-COS conjugates

PBS buffer (10 mM, pH 7.0) was used to dilute the FG and FG-COS conjugates to 10 mg/mL and 20 mL sample solution was taken into a 50 mL centrifuge tube. After homogenizing at a high speed of 20000 rpm for 60 s, the foam volume at 1 min and 5 min was measured and recorded as V_1 and V_5, respectively. The foaming activity index (FA) and foaming stability index (FS) were calculated by the following formulas:

$$FA\ (\%) = V_1/20 \times 100\% \quad (4)$$

$$FS\ (\%) = V_5/V_1 \times 100\% \quad (5)$$

2.3.7. Determination of surface hydrophobicity of FG/FG-COS conjugates

The hydrophobicity (H_0) of FG and FG-COS conjugates were measured by the ANS probe method (Haskard et al., 1998). From the prepared 1 mg/mL FG and FG-COS conjugates solution, 0.16–0.96 mL was taken into the centrifuge tube, and then PBS buffer (10 mM, pH 7.0) was added to a total volume of 4 mL. The final concentration of the two samples were 0.04–0.24 mg/mL 20 μL ANS solution was immediately added and mixed. The fluorescence intensity was measured with a fluorescence spectrophotometer (Fluoromax-4C-L, Horiba Instrument Inc) after 5 min of reaction in the dark. The conditions were set as follows: excitation wavelength was 390 nm, emission wavelength was 470 nm and slit width was 5 nm. The ordinate was the fluorescence intensity (CPS), the abscissa was the sample concentration (mg/mL), and the slope of the fitting curve was the surface hydrophobicity H_0.

2.3.8. Determination of sulfhydryl content of FG/FG-COS conjugates

The determination of sulfhydryl content referred to the method of Chen et al. (2019b) with a little adjustment. In short, 25 mg/mL FG and FG-COS conjugates were prepared, and then diluted with reagent A (containing 8 M urea, 0.09 M glycine, 0.086 M Tris, 0.004 M EDTA, pH adjusted to 8.0) to 3 mg/mL as the sample solution. 5 mL of the two samples solution and 50 μL of reagent B (4 mg/mL DTNB, dissolved in reagent A) were mixed vigorously for a few seconds, and then reacted for 1 h at room temperature under dark conditions. Ultraviolet spectrophotometer was used to measure the absorbance of the samples at a wavelength of 412 nm to determine the extinction coefficient. The sulfhydryl content was calculated by formula as follows:

$$SH\ (\mu mol/g) = 73.53\ \mu M \times A_{412} \times D/C \quad (6)$$

Where 73.53 μM = 106 μ/(L•cm)/13600 $M^{-1}cm^{-1}$, D was the dilution factor of the sample solution, and C was the sample solution's concentration. For the blank group, deionized water was used to replace the initial sample solution.

2.3.9. DPPH radical scavenging rate of FG/FG-COS conjugates

The specific experiment was the same as described in section 2.2.2, and the solution was diluted to 0.5–2.5 mg/mL respectively. According to the linear relationship between sample concentration and DPPH radical scavenging rate, the EC_{50} value was obtained.

2.3.10. The reducing power of FG/FG-COS conjugates

The reducing power of FG, COS, FG-COS conjugates were evaluated by the method of Mohammadian et al. (2021). Took 1 mL of samples of different concentrations, dissolved in 2.5 mL of phosphate buffer (0.2 M, pH 6.6), and 2.5 mL of 1% $K_3[Fe(CN)_6]$. Incubated in a 50 °C water bath for 20 min before being quickly immersed in cold water to cool. Then, added 2.5 mL of 10% TCA and mixed well. 10 min centrifuged at 3000 rpm. 2.5 mL of supernatant was combined with 2.5 mL of distilled water and 0.5 mL of 0.1% $FeCl_3$ solution. After standing still for 10 min, the absorbance was measured at 700 nm and recorded as A. 1 mL deionized water instead of sample solution was used and set as blank group, and the absorbance value was measured and recorded as A_0. The reducing power and the absorbance value were positively correlated, and finally the absorbance value $A\text{-}A_0$ represented the reducing power.

2.4. Fabrication of curcumin-loaded FG-COS conjugates (FG–COS–Cur)

Refer to the method reported by Cai et al. (2021) with a sightly modification. Cur of different concentrations dissolved in absolute ethanol was added dropwise to the FG-COS conjugates solution (1 mg/mL in the centrifuge tubes) under vortexed with a Vortex mixer for 2 min in the dark to form FG–COS–Cur nanoparticles (adjust pH to 6). To remove the absolute ethanol, left them open overnight in the dark. The free Cur was then isolated using centrifugation (10,000 rpm, 10 min) and redissolved in the same volume of ethanol. An UV spectrophotometer was used to measure the concentration of free Cur using a standard curve of absorbance at 426 nm. The following formulas were used to compute the Cur encapsulation efficiency (EE) and loading amount (LA):

$$EE\ (\%) = (\text{Loaded amount of Cur/Total amount of Cur}) \times 100\% \quad (7)$$

$$LA\ (\%) = (\text{Loaded amount of Cur/Total amount of FG–COS–Cur}) \times 100\% \quad (8)$$

2.5. Characterization of FG–COS–Cur

2.5.1. Particle size and PDI

A Malvern particle size analyzer (Nano-2, Malvern Instruments) was used to determine the FG–COS–Cur nanoparticles particle size, PDI and size distribution peaks. Particle size was read in terms of z-average and size distribution was read in terms of intensity. All measurements were done at 25 °C, and each report's results were the average of the three groups of testing.

2.5.2. Curcumin degradation in the presence of UV irradiation

Free Cur and FG–COS–Cur nanoparticles with Cur concentrations of 20 μg/mL were irradiated with ultraviolet light for 8 h. The absorbance of the remaining Cur in the solution was measured in real time at different time intervals using an ultraviolet spectrophotometer, and real-time Cur absorbance value was divided by the original solution Cur absorbance to calculate retention rate.

2.5.3. Placement stability

Preparation and determination of FG–COS–Cur nanoparticles with different Cur concentrations according to the above method (section 2.5.1), then continued to measure the particle size, PDI and size distribution peaks of the sample after standing for 24 h in the room temperature. Particle size was read in terms of z-average and size distribution was read in terms of intensity.

2.5.4. Scanning electron microscope (SEM)

Prepared FG–COS–Cur nanoparticles with the Cur concentration of 20 μg/mL and diluted it 10 times, then according to section 2.3.2 and using a scanning electron microscope with ultra-high resolution field emission (Verios G4, Thermo Fisher Scientific Inc) to observe the morphology.

2.5.5. Intrinsic fluorescence spectra

The interaction between FG-COS conjugates and Cur was evaluated by protein intrinsic fluorescence spectroscopy (Zhu et al., 2017). The determination of Intrinsic fluorescence spectra referred to the method of Liu et al. (2018) with a little adjustment. The initial Cur solution (2 mg/mL) was prepared in ethanol absolute, and then added dropwise to the FG-COS conjugates until the nanoparticles reached the desired Cur concentrations from 0 to 20 μg/mL. The FG–COS–Cur solution was further vortexed for 2 min to ensure complete formation of the nanoparticles. The emission spectra from 380 to 500 nm were recorded at an excitation wavelength of 280 nm. The excitation and emission slits

widths were set to 3.6 nm and appropriate blank corresponding to the free Cur and ultrapure water was subtracted as background.

The Stern-Volmer equation was used to further investigate the quenching of protein intrinsic fluorescence:

$$F_0/F = 1+K_{sv}[Q] = 1+k_q\tau_0[Q] \quad (9)$$

In the formula, F_0 and F were the fluorescence intensities without or with a Cur, respectively. [Q] was the Cur concentration (μM), k_q was the quenching rate constant, τ_0 was the fluorescence lifetime of the fluorescent substance, which equal to 10^{-8} s, K_{sv} was the quenching constant of the Stern-Volmer equation.

2.5.6. Fourier transform infrared spectroscopy

The sample of FG–COS–Cur, FG-COS conjugates and Cur were prepared and the next steps refer to section 2.3.3.

2.5.7. X-ray diffraction

Refer the method in section 2.3.4, the crystal states of the powder samples (FG–COS–Cur, FG-COS conjugates and Cur) were analyzed by Xpert3. Continuously scan the sample from 4° to 70° at a speed of 4°/min.

2.5.8. DPPH radical scavenging rate of free Cur and FG–COS–Cur

The specific experiment method was the same as that in section 2.2.2.

2.5.9. ABTS radical scavenging ability of free Cur and FG–COS–Cur

The ABTS radical scavenging ability of all samples were estimated according to the method of Wang et al. (2012) with a sightly modification. Prepared ABTS stock solution (7 mM) and $K_2S_2O_8$ solution (2.45 mM), mixed them in a ratio of 1:1 and placed in the dark for 16 h. The ABTS radical solution was diluted to an absorbance of 0.70 ± 0.02 at 734 nm in phosphate buffer (5 mM, pH 7.4). The ABTS free radical solution was mixed with different concentrations of samples at the ratio of 10:1. After reacting for 10 min, the absorbance was measured at 734 nm. The ABTS radical scavenging activity of the sample was determined as follows:

$$\text{ABTS radical scavenging ability (\%)} = [(A_{control}\text{-}A_{sample}) / A_{control}] \times 100\% \quad (10)$$

2.5.10. Reducing power of free Cur and FG-MPRs-Cur

Different concentrations of Cur and FG–COS–Cur nanoparticles were prepared, and then refer the method in section 2.3.10 to determine the reducing power.

2.6. Evaluating the antioxidant capacity of FG–COS–Cur on Caco-2 cells

2.6.1. Cytotoxicity

The viability of Caco-2 cells were measured by MTT assay. Caco-2 cells were seeded in 96-well plate in DMEM containing 20% FBS, 1% penicillin-streptomycin mixture and 1% non-essential amino acid solution with a plating density of 5×10^4 cells/well, then placed the plate in a 37 °C, 5% CO_2 incubator for 24 h. Prepare the Cur stock solution (dissolved in DMSO) and add dropwise to PBS (free Cur) and FG-COS conjugates (FG–COS–Cur) to achieve the desired Cur concentration. Then cells were incubated with different concentrations of Cur, FG-COS conjugates and FG–COS–Cur nanoparticles. After 24 h of incubation, the 20 μL of MTT solution (5 mg/mL in PBS) was added, and continued to incubate for 4 h. Then, discarding the supernatant carefully and adding 150 μL of DMSO to each well. After 600 rpm microplate shaker for 10 min, the absorbance was determined at 570 nm wavelength with multifunctional microplate reader (SpectraMax iD3, Molecular Devices Inc) and the viability of the cells was determined using the following equation:

$$\text{Cell viability (\%)} = (A_{sample} / A_{control}) \times 100\% \quad (11)$$

2.6.2. Cellular uptake study of FG–COS–Cur nanoparticles on Caco-2 cells

Caco-2 cells were seeded in 6 well plates at a seeding density of 2×10^5 placed in incubator. Changed the medium every day and cultured for 3 days. At this point, the cells cover the entire well plate. Then, co-incubation with cells by adding different concentrations of Cur and FG–COS–Cur. After incubated for 6 h in an incubator, the supernatant was carefully discarded, and the cells were washed twice in PBS solution to remove any unabsorbed Cur. Then added 1% Triton solution (200 μL per well) and allowed it to stand for 3 min to fully lyse the cells. Then, using a microplate reader to measure the fluorescence under the conditions of excitation and emission wavelengths of 425 nm and 528 nm, respectively.

2.6.3. Establishment of H_2O_2-induced oxidative damage model of Caco-2 cells

In order to choose the optimal concentration of H_2O_2 for inducing oxidative damage of Caco-2 cells, referring the method reported by Yang et al. (2019) and with slight modifications. The experiment included the control group and the H_2O_2 oxidative damage model group. In the H_2O_2 oxidative damage model group, each well was added with DMEM growth medium containing different concentrations of H_2O_2 (final concentrations of H_2O_2 were 100, 200, 400, 650, 1000, 1500 and 2000 μM respectively), while the control group was replaced by PBS. The treated cells were cultured for 4 h, removed H_2O_2-containing medium and the cell viability was detected by the MTT method.

2.6.4. Determination of cell viability of H_2O_2-induced oxidative damage in Caco-2 cells

Refer to the method reported by Liang et al. (2019) to analyze the protective effects of Cur and FG–COS–Cur nanoparticles on the oxidative damage caused by H_2O_2 in Caco-2. The experiment included blank group, control group and sample treatment antioxidant group. The oxidative damage model of Caco-2 cells induced by H_2O_2 was established according to section 2.6.3. Subsequently, the antioxidant group cells were cultured in the presence of different final concentrations of free Cur and FG–COS–Cur nanoparticles (5, 10, and 20 μg/mL of Cur, respectively) for 24 h while the blank group and the control group were replaced with PBS. After the incubation, cell viability was tested by MTT assay.

2.6.5. Determination of ROS content of H_2O_2-induced oxidative damage in Caco-2 cells

Caco-2 cells were seeded on a 6-well plate and H_2O_2-induced oxidative damage of Caco-2 cells model was established. The experiment was divided into a blank control group (PBS) and a sample protection group (FG–COS–Cur nanoparticles at final Cur concentrations of 2.5, 5, 10, 20 μg/mL). After 24 h of incubation in the incubator, followed ROS detection kit manual operation steps to determine the fluorescence intensity of each well.

2.6.6. Determination of extracellular lactate dehydrogenase content of H_2O_2-induced oxidative damage in Caco-2 cells

Using the method in section 2.6.3 to inoculate Caco-2 cells into a 6-well plate and induced oxidative damage model. After adding samples and incubating for 24 h, centrifuged at 2000 rpm for 15 min to collect the supernatant. Then determined the absorbance value of each well to measure the LDH activity using a commercial kit and following the manufacturer's instructions.

2.6.7. Determination of intracellular superoxide dismutase and catalase content of H_2O_2-induced oxidative damage in Caco-2 cells

Using the method in section 2.6.3 to inoculate Caco-2 cells into a 6-well plate and induced oxidative damage model. After adding samples and incubating for 24 h, cells were gathered and lysed by ultrasonic cell crusher. Then measured the SOD, CAT activity and protein content using a commercial kit (Jiancheng, Nanjing, China).

2.7. Data analysis

The statistical analysis was performed by SPSS Statistics 26 software to analyze the variance. All data was presented as means standard deviations. One-way analysis of variance with Duncan's multiple range tests was used to establish statistical significance, with a result of $p < 0.05$ being statistically significant. Different lowercase letters represented as significant difference at $p < 0.05$. *$p < 0.05$ significant change; **$p < 0.01$; ***$p < 0.001$.

3. Results and discussion

3.1. Screening of Maillard reaction of FG and COS

The formation of intermediate products were indicated by the $A_{294\ nm}$ during the Maillard reaction, whereas the formation of end products were shown by the $A_{420\ nm}$. The increase in absorbance at 294 nm and browning coincided with an increase in antioxidative activity (Benjakul et al., 2005). Therefore, $A_{294\ nm}$, $A_{420\ nm}$ and DPPH radical scavenging rate were usually used as the main indicators to determine the Maillard reaction conditions. The Maillard reaction of FG and COS was carried out by the moist heat method. The DPPH radical scavenging rate, $A_{294\ nm}$ and $A_{420\ nm}$ were used as monitoring and optimization indicators (Fig. 1). With the increased of reaction times, the values of $A_{294\ nm}$ and $A_{420\ nm}$ increased gradually, indicating that the degree of the Maillard reaction and the reaction products increased. The DPPH free radical scavenging rate reached a maximum when the reaction time was at 4 h and then leveled off (Fig. 1A). With the increased of temperature, the DPPH free radical scavenging rate increased initially and then stabilize.

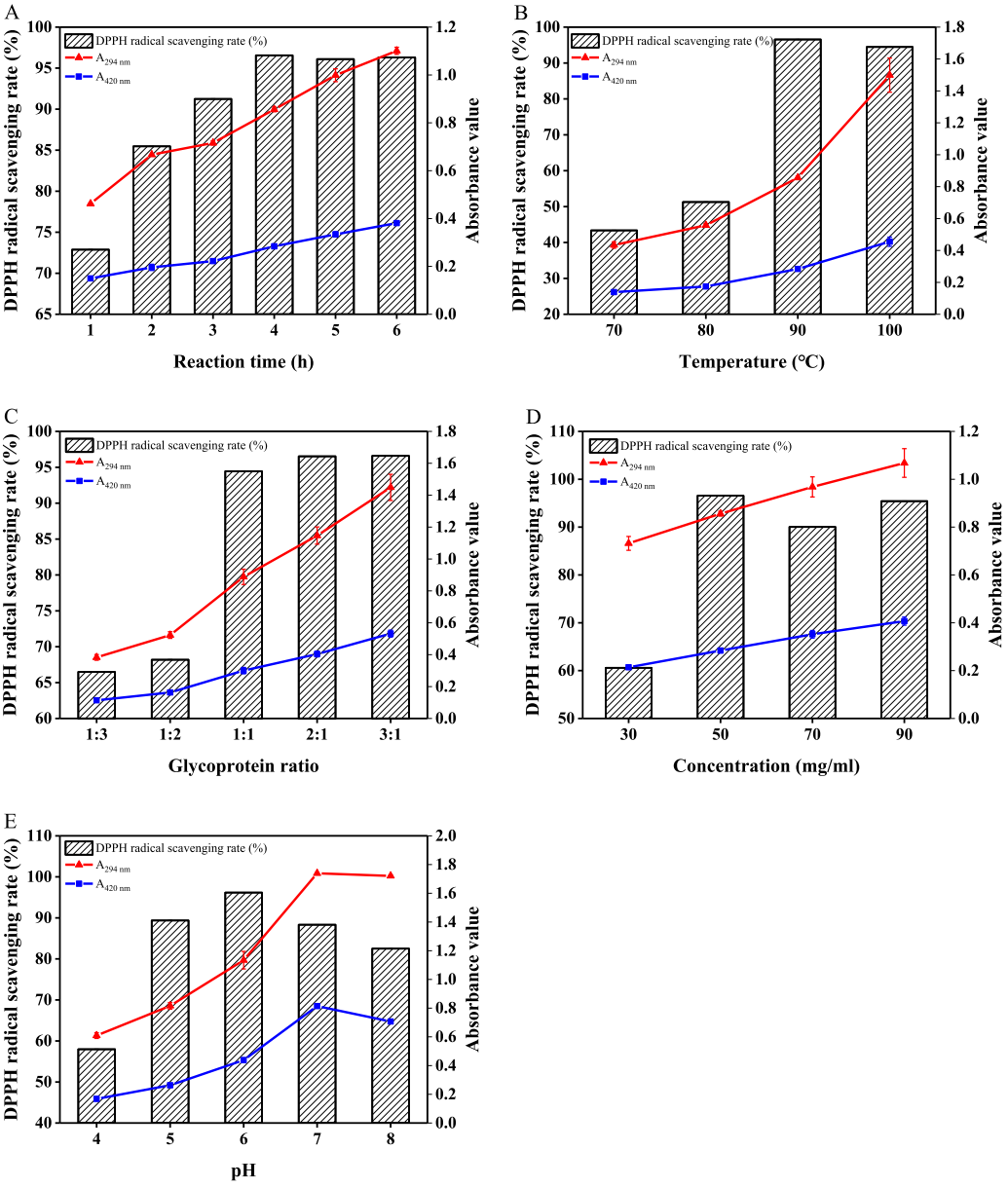

Fig. 1. The effect of (A) Reaction time (B) Temperature (C) Glycoprotein ratio (D) Concentration (E) Initial pH on the Maillard reaction of FG/COS.

At 90 °C, the DPPH free radical scavenging rate reached a maximum (Fig. 1B). As for glycoprotein ratio and concentration, the DPPH free radical scavenging rate reached a higher level when glycoprotein ratio and concentration were 1:1 and 50 mg/mL. Increasing the ratio of COS and concentration did not significantly alter the DPPH free radical scavenging rate (Fig. 1C–D). It was worth noting that there were some differences in the rate between $A_{294\ nm}$ and $A_{420\ nm}$. The increasing rate of $A_{294\ nm}$ was greater than $A_{420\ nm}$, which was linearly reaction time, temperature, glycoprotein ratio and concentration-dependent (Fig. 1A–D). When the pH changed from acidic to neutral, it was found that the values of $A_{294\ nm}$ and $A_{420\ nm}$ increased, while the pH was from neutral to alkaline, the values of $A_{294\ nm}$ and $A_{420\ nm}$ decreased (Fig. 1E). Meanwhile, at the pH 6, the DPPH free radical scavenging rate was the highest, which suggested that it had better antioxidant properties (Fig. 1E). According to the above results, the reaction time, temperature, glycoprotein ratio, concentration and pH were determined to be 4 h, 90 °C, 1:1, 50 mg/mL and pH 6, respectively.

3.2. Characterization of FG-COS conjugates

3.2.1. Micromorphology of FG-COS conjugates

AFM was an ideal mean to effectively observe the microstructure and surface morphology of nanocomplexes. AFM scans of FG-COS conjugates revealed irregular three-dimensional structures or roughly spherical forms (Fig. 2A–B). But compared with the spherical aggregated and irregular aggregated of FG (Sow et al., 2019), it could be judged that the structure of FG had undergone further curled and folded change after Maillard reaction to form smaller particles. The SEM image showed that the microscopic morphology of FG-COS conjugates were round and nearly spherical shape, but varies of different sizes (Fig. 2C). Combined with the AFM and SEM image, the microscopic morphology of FG-COS conjugates were almost spherical.

3.2.2. Fourier transform infrared spectroscopy

For studying the structural features of protein/polysaccharides complexes, FTIR spectroscopy was an effective technique (Han et al., 2017). During the Maillard reaction, free amino groups in protein molecules could form covalent bonds with the carbonyl groups of carbohydrate, which led to change in the infrared spectrum. The FTIR spectra of FG, COS and FG-COS conjugates were shown in Fig. 3A. The characteristic absorption bands of O–H and C–H groups of COS were 3200–3400 cm^{-1} and 3000-2800 cm^{-1}, respectively (Wang et al., 2014). The absorption bands at approximately 1400 cm^{-1} and 1600 cm^{-1} were attributed to the symmetric and asymmetric COO- groups stretching vibrations, which confirmed the existence of COS. Compared to FG, FG-COS conjugates had stronger absorption in the region of 1180–1000 cm^{-1}. The absorption in this region was caused by the bending vibration of C–O–H in COS and the extensional vibration of C–C and C–O (Guerrero et al., 2013), usually called the "sugar" band, was the strongest band in the mid-infrared spectrum, and these absorptions were weak in the spectrum of most proteins (Oliver et al., 2009). The region of 1630–1660 cm^{-1} in the FG-COS conjugates spectrum showed strong C–N stretching vibration, which was caused by the Maillard reaction (Su et al., 2010; Wang et al., 2014; Yang et al., 2015). The Maillard reaction between FG and COS was accompanied by chemical reactions, which affected infrared spectrum. This phenomenon possibly due to the consumption of some functional groups and the emergence of others, which indicated that COS was attached to FG and changed the chemical structure of FG (Zhang et al., 2017).

3.2.3. X-ray diffraction analysis (XRD)

XRD was used to evaluate structural modification and molecular conformation changed caused by the Maillard reaction (Kchaou et al., 2019). The XRD spectra of FG-COS conjugates, COS and FG were shown in Fig. 3B. Compared with FG, the peaks of FG-COS conjugates were flatter and wider, which meant FG and COS had good compatibility,

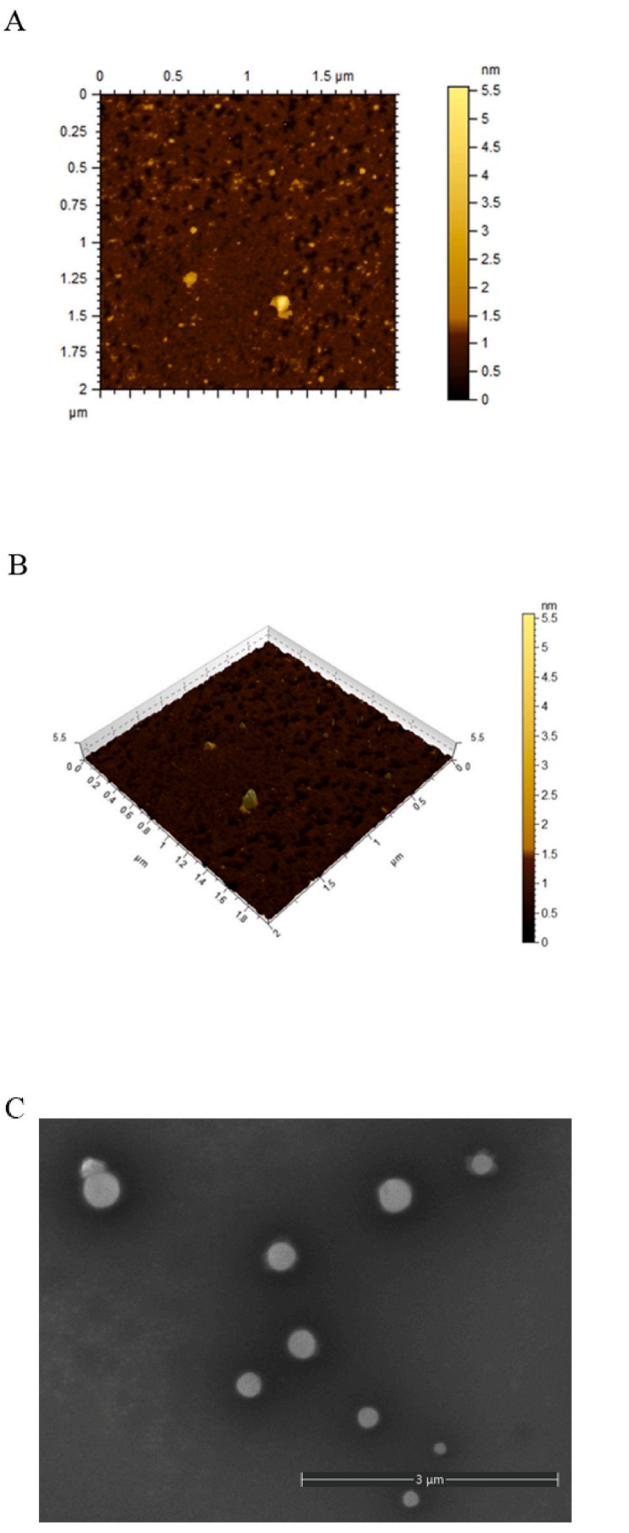

Fig. 2. Micromorphology of FG-COS conjugates. (A, B) Atomic force microscope image of FG-COS conjugates (C) Scanning electron micrograph image of FG-COS conjugates (Scale bar:3 μm).

indicating that the original crystalline domain of FG was progressively destroyed by COS. Similar results on protein/carbohydrate complexes were found (Yang et al., 2015). In the COS spectrum, the diffraction peaks at 13° and 21° were observed, while in FG-COS conjugates, the diffraction peaks of COS disappeared, indicating that the structure of COS and FG was destroyed and an interaction occurred to form a new

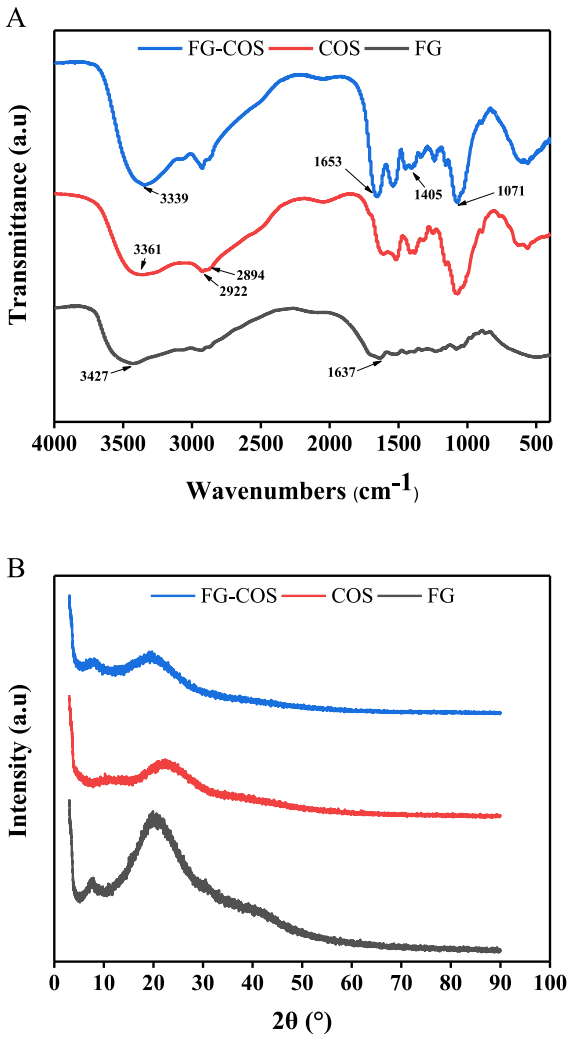

Fig. 3. Interaction between FG and COS. (A) Fourier transform infrared spectroscopy of FG-COS conjugates, COS and FG (B) X-ray diffraction analysis of FG-COS conjugates, COS and FG.

substance (Luo et al., 2013). Heat treatment could alter the structural and functional properties of proteins, resulting in denaturation due to the disruption of forces that stabilized the native conformation, such as hydrogen bonds, electrostatic force and hydrophobic bonds (Pirestani et al., 2018).

3.2.4. Emulsifying and foaming properties of FG/FG-COS conjugates

From Table 1, it could be seen that the EAI and ESI of FG-COS conjugates were significantly improved after the Maillard reaction, which were 8.34 ± 0.96 m^2/g and 20.83 ± 0.30 min, respectively. Glycosylated fish gelatin could delay the flocculation of emulsion droplets during storage, one possible reason was that polysaccharides might improve the protein emulsion characteristics by reducing aggregation and coalescence (Zhu et al., 2010). And because of the better emulsification properties of glycosylated fish gelatin, it could be used in coffee applications instead of milk as a novel coffee whitener (Huang et al., 2020). After glycosylation, foaming activity (FA) and foaming stability (FS) were significantly reduced (Table 1). Gharbi and Labbafi (2019) showed that glycosylation led to unfolding of some proteins and increased solubility, which could improve foaming performance, but excessive glycosylation of proteins would increase the steric hindrance between complex's molecular chains, resulting in reducing foaming performance.

3.2.5. Surface hydrophobicity and sulfhydryl content of FG/FG-COS conjugates

The H_0 index revealed the number of hydrophobic groups on the protein surface in contact with the surrounding environment, which was directly related to emulsifying capabilities of protein (Zhang et al., 2013). As shown in Table 2, after the Maillard reaction, the surface hydrophobicity increased from 3.96 × 10^5 to 318.83 × 10^5, and the sulfhydryl content increased from 3.06 μmol/g to 104.53 μmol/g. FG-COS conjugates subjected to Maillard reaction displayed markedly higher surface hydrophobicity than FG, probably due to aggregate dissociation or protein unfolding (Chen et al., 2019a). High temperature conditions promoted the exposure of the hydrophobic groups of FG that were located inside the molecule in their native form (Spotti et al., 2019). After the Maillard reaction between protein and carbohydrate, sulfhydryl groups were exposed, and the exposed sulfhydryl groups could scavenge free radicals, thereby enhancing antioxidant activity (Wu et al., 2018). Sun et al. (2022) reported that Maillard process was able to unfold the SPI structure, probably because the tryptophan group encapsulated inside the protein structure was exposed, thereby increasing its surface hydrophobicity (Stanciuc et al., 2015).

3.2.6. Evaluation of antioxidant activity of FG/FG-COS conjugates

MRPs had strong antioxidant properties and could protect food functional factors from oxidative degradation (Shi et al., 2019). The antioxidant property of FG-COS conjugates mainly came from COS and MRPs. The precise radical scavenging mechanism of COS was inferred that the unstable free radicals might react with amino or hydroxyl groups in pyranose rings, and formed stable macromolecule radicals (Kim et al., 2005). The DPPH radical scavenging rate of FG-COS conjugates, COS and FG at different concentrations were illustrated in Fig. 4A. The FG-COS conjugates and COS showed a higher DPPH scavenging rate than FG. The DPPH scavenging activity of FG-COS conjugates were 74.39% and COS was 69.33%, which was higher than of FG (12.90%) when the concentration was 2 mg/mL. According to the equation calculated from the linear function relationship, the EC_{50} value of COS was 1.436 mg/mL and the EC_{50} value of FG-COS conjugates were 1.292 mg/mL. Moreover, the mass ratio of COS and FG reaction in FG-COS conjugate was 1:1, which meant that under the same quality, the COS in FG-COS conjugates was half less compared with pure COS. However, FG-COS conjugate was stronger than COS in antioxidant capacity, which indicating that half of the amount of COS through the Maillard reaction can achieve the antioxidant capacity of pure COS (without participating in the Maillard reaction). That was to say, Maillard reaction improved the antioxidant properties of COS and FG in vitro. Similar results were found that the DPPH radical scavenging activity of COS–Gly–MRPs increased after the Maillard reaction (Yan et al., 2018).

The reducing power was proportional to the absorbance. From Fig. 4B, in the concentration range of 4–12 mg/mL, the FG-COS

Table 1
Emulsification ability and foaming ability of FG/FG-COS conjugates.

	EAI (m^2/g)	ESI (min)	FA (%)	FS (%)
FG	4.80 ± 0.50	14.38 ± 0.80	120.00 ± 5.00	61.12 ± 1.27
FG-COS	8.34 ± 0.96***	20.83 ± 0.30***	55.00 ± 8.66***	46.15 ± 6.66*

Note: *p < 0.05 significant change; **p < 0.01; ***p < 0.001.

Table 2
Surface hydrophobicity and sulfhydryl group content of FG/FG-COS conjugates.

	H_0 index (× 10^5)	SH μmol/g
FG	3.96 ± 0.04	3.06 ± 0.41
FG-COS	318.83 ± 7.07***	104.53 ± 0.74***

Note: *p < 0.05 significant change; **p < 0.01; ***p < 0.001.

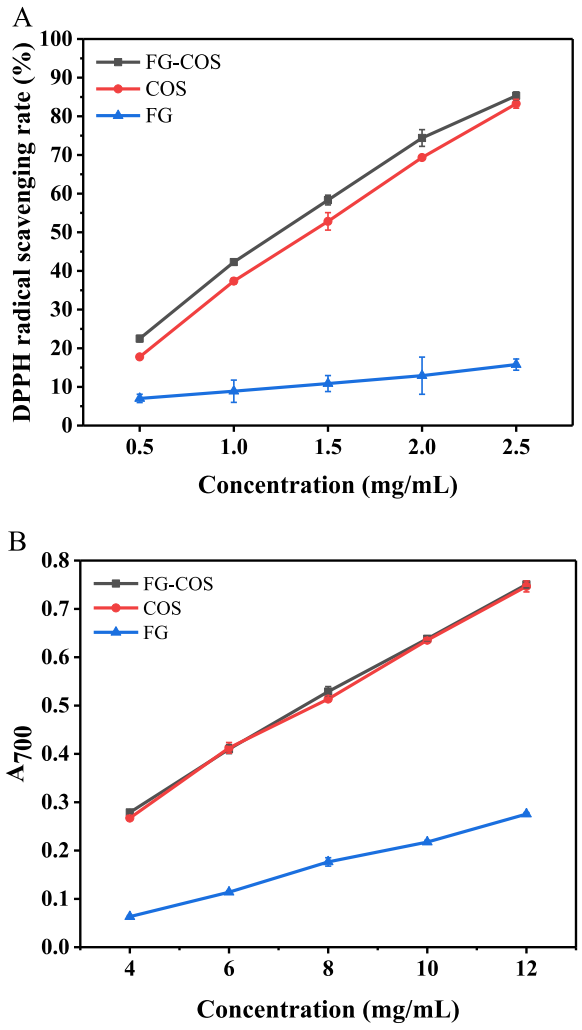

Fig. 4. Antioxidative capacity of FG-COS conjugates, COS and FG. (A) DPPH radical scavenging rate (B) reducing power.

conjugates and COS showed a higher reducing power than FG, similarly. The reducing power absorbance of FG-COS conjugates at 4 mg/mL was 1.04- and 4.41-fold that of COS and FG at the same concentration, respectively. Owing to FG-COS conjugate was prepared by mixing FG and COS in equal ratio, which meant that under the same mass, the COS content of FG-COS was only half of that of pure COS. However, the results showed that half the amount of COS through Maillard reaction could achieve better antioxidant capacity than pure COS. This might be because of the amadori degradation products produced by Maillard reaction, heterocyclic compounds and the hydroxyl groups of pyridone in melanoidin, which could provide electrons to block free radical-mediated chain reactions (Yoshimura et al., 1997). Either intermediates or the final products could act as hydrogen donors during Maillard reaction, which gave FG-COS conjugates high radical scavenging activity (Eric et al., 2013).

3.3. Characterization of FG–COS–Cur

3.3.1. The formation and stability of FG–COS–Cur nanoparticles

Based on the significantly improved hydrophobicity, we tried to encapsulate the hydrophobic functional molecule Cur into FG-COS conjugates. The FG–COS–Cur nanoparticles were fabricated by anti-solvent coprecipitation method which was the most common and simple ways to encapsulate Cur. The Cur EE and LA of FG-COS conjugates were above 89% and 2.5% respectively, when the Cur concentration was 20 μg/mL (Fig. 5A). Besides, the EE and LA will decrease when the concentration of Cur above 20 μg/mL. The stability of colloidal particles in solution was closely related to the size of colloidal particles. Results of Fig. 5B showed that the particle size stayed nearly unchanged when the Cur concentration increased up to 10 μg/mL, then reduced at 20–30 μg/mL, but increased at 40 μg/mL. While the PDI value steadily declined as Cur concentration increased up to 30 μg/mL, it drastically increased at 40 μg/mL. It can be inferred that Cur molecules most likely formed smaller homogeneous aggregates with FG-COS conjugates at 20–30 μg/mL, and excessive surface adsorption of Cur occurred at 40 μg/mL. The sizes distribution of the different concentration of Cur in FG-COS conjugates, as determined by Malvern analyzer, were shown in Fig. S1. The particle size of FG–COS–Cur nanoparticles presented a single peak in the range of concentration of Cur was 8 μg/mL-30 μg/mL. With the continued increased of the concentrations of Cur, aggregates started to appear and presented multiple peaks.

The loss of hydrogen atoms from a highly activated carbon atom in keto form caused free Cur to be light-sensitive (Yi et al., 2021). Cur retention rate in FG–COS–Cur nanoparticles and free Cur under UV light were shown in Fig. 5C. Although the retention rate of Cur and FG–COS–Cur nanoparticles gradually decreased under ultraviolet light, the rate of FG–COS–Cur nanoparticles were always higher than free Cur. Especially under 8 h ultraviolet radiation, the retention rate of Cur in FG–COS–Cur nanoparticles were remain above 80%. A similar situation was also observed in previous researches (Zhang et al., 2022). The improved photostability of Cur might be due to the antioxidant effect of FG-COS conjugates, which prevented the UV-induced loss of hydrogen protons of Cur (Cai et al., 2021).

The FG–COS–Cur nanoparticles were placed at room temperature for 24 h in the dark. The particle sizes changed were used as the evaluation index to investigate the storage stability of different concentrations of Cur in FG–COS–Cur nanoparticles (Fig. 5D). Under different Cur concentrations, the particle sizes of FG–COS–Cur nanoparticles increased after being placed for 24 h. When the concentrations of Cur below 20 μg/mL, adding Cur could reduce the particles size increased, which probably because the molecules may be inside of FG-COS conjugates and remained compact. However, when the concentrations of Cur more than 20 μg/mL, the particle size increased significantly faster after 24 h placement. The high increase in size at 40 μg/mL was most likely owing to the complexes being readily stretched over time because of increased surface adsorbed Cur molecules. It is worth noting that the FG–COS–Cur particle size distribution after 24 h was most similar to the original distribution (Cur concentration was 20 μg/mL) (Fig. S2), and the overall particle size increase was the smallest (Fig. 5B). Therefore, the ideal loading concentrations of Cur on FG-COS conjugates should be 20 μg/mL. Finally, FG–COS–Cur nanoparticles morphology with 20 μg/mL of Cur was examined by using SEM. FG–COS–Cur granules mostly showed spherical shapes with a diameter of approximately 150 nm but some were irregular (Fig. 5E–F). Incorporation of Cur did not greatly modify the shape of the FG-COS conjugates, but the particle size and polydispersity had decreased (Fig. 5B).

3.3.2. Fluorescence measurement

Protein endogenous fluorescence was mostly caused by amino acid residues like tryptophan, tyrosine, and phenylalanine (Dezhampanah et al., 2022). The fluorescence quenching of Cur on protein could be analyzed by fluorescence spectroscopy. The fluorescence gradually decreased with the addition of increasing the concentrations of Cur, indicating the interaction between Cur and FG-COS conjugates (Fig. 6A) (Yue et al., 2008). This might due to the fact that Cur could cause fluorescence quenching of amino acids.

The quenching mechanism could be static (complex formation) or dynamic (molecular collision) (Wang et al., 2018) and the Stern-Volmer equation could be used to analyze the quenching procedure (Chung et al., 2016). Studies had shown that the maximum dynamic quenching

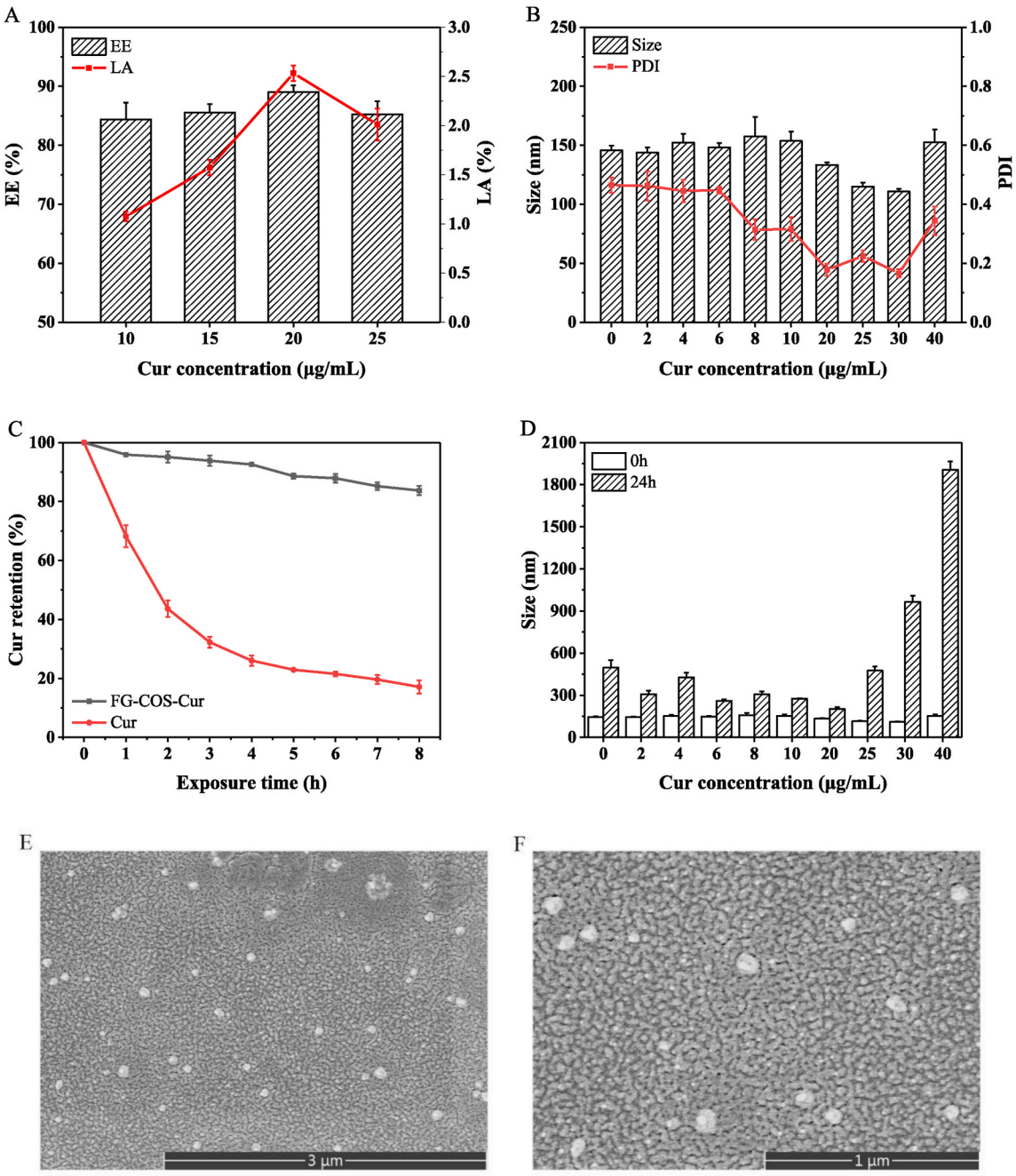

Fig. 5. Characterization of curcumin-loaded nanoparticle (FG–COS–Cur nanoparticle). (A) The encapsulation efficiency and loading amount of FG–COS–Cur nanoparticle (B) The particles properties of FG–COS–Cur nanoparticle with different concentrations of Cur. (C) Retention rate of Cur in FG–COS–Cur nanoparticle and free Cur under UV irradiation. (D) The 24 h placement stability of FG–COS–Cur nanoparticle with different Cur concentrations. (E, F) Scanning electron micrograph image of FG–COS–Cur nanoparticle (Scale bar: 3 μm and 1 μm, respectively).

constant of various endogenous fluorescence quenchers for biological macromolecules was 2.0×10^{10} M^{-1} S^{-1} and the k_q value of the interaction between Cur and FG-COS conjugates (3.7898×10^{12} M^{-1} S^{-1} from Table 3) was much greater than the maximum dynamic quenching constant, which indicated that the fluorescence quenching of FG-COS conjugates by Cur was static quenching.

The binding capacity could be calculated from the following equation:

$$\log[(F_0\text{–}F)/F] = \log K_a + n\log[Q] \quad (12)$$

Where Ka was the binding constant and n was the number of binding sites.

As shown in Table 3, the curves of binding affinity showed the good linear relationships ($R^2 > 0.99$). The conjugation of FG-COS conjugates with Cur was characterized as moderate binding (K_a ranging from 10^5 to 10^6 M^{-1}) in comparison to complexes with significant affinity ranging from 10^6 to 10^8 M^{-1} (Belatik et al., 2012; Zhu et al., 2017). The number of binding sites was almost equivalent to one, indicating that during the interaction, there was approximately one binding site in FG-COS conjugates for Cur binding. These results were similar to our previous reports (Weng et al., 2019).

3.3.3. *Fourier infrared spectroscopy measurement*

The FT-IR spectra of FG–COS–Cur, FG-COS conjugates and Cur were

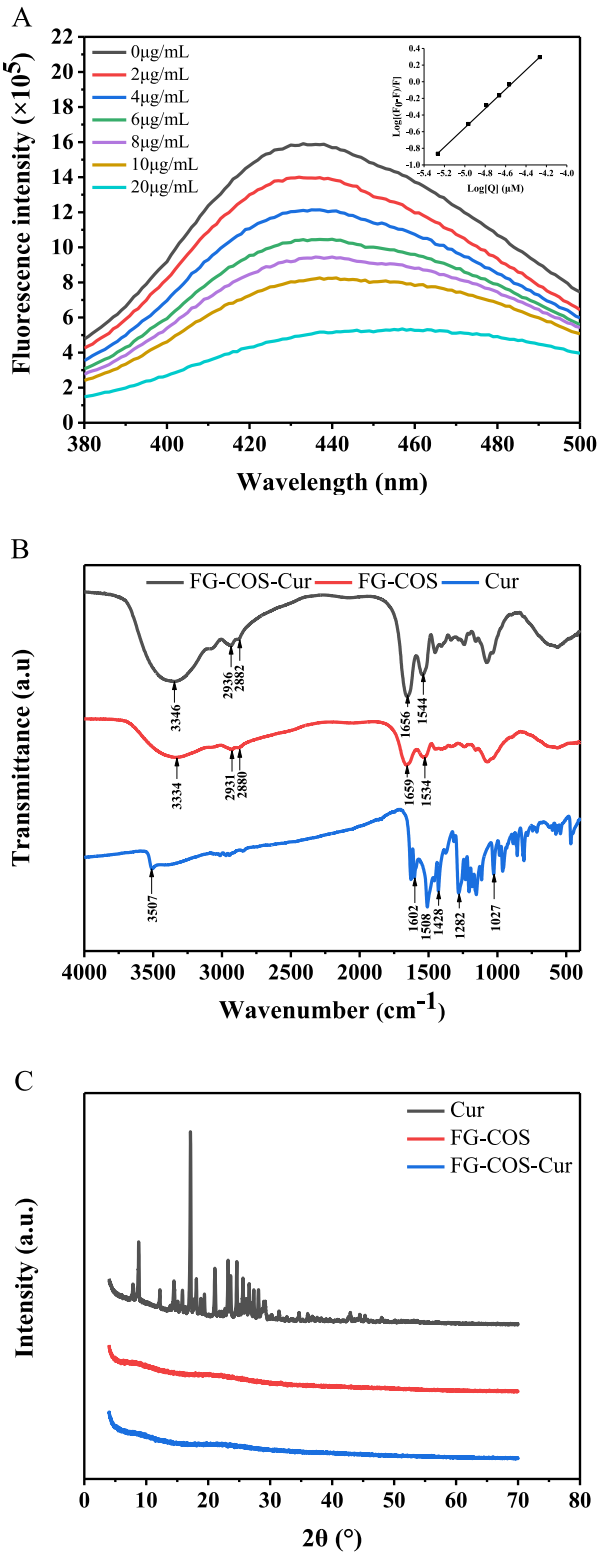

Fig. 6. Interaction between FG-COS conjugates and Cur. (A) Fluorescence spectra of FG-COS conjugates with different concentrations of Cur (Inside: The Stern-Volmer Equation) (B) Fourier transform infrared spectroscopy of FG–COS–Cur, FG-COS conjugates and Cur (C) X-ray diffraction pattern of FG–COS–Cur, FG-COS conjugates and Cur.

Table 3
The parameters of Cur interaction with proteins in the Stern-Volmer Equation.

K_{sv} (M^{-1})	K_q (× 10^{12} $M^{-1}S^{-1}$)	R^2	K_a (M^{-1})	n	R^2
37898	3.7898	0.9987	184331.6879	1.1628	0.9991

displayed in Fig. 6B. The characteristic absorption peak of Cur at 3507 cm^{-1} was the stretching vibration of phenolic hydroxyl-OH. The absorption band at 1602 cm^{-1} were C═C stretching vibration and C═O stretching vibration, and at 1508 cm^{-1} was C–C–C in-plane bending vibration (Bourbon et al., 2016). In the FG–COS–Cur, the characteristic peaks of Cur at wave numbers 3507 cm^{-1}, 1602 cm^{-1}, 1508 cm^{-1}, 1428 cm^{-1}, 1282 cm^{-1} and 1027 cm^{-1} disappeared, indicating that Cur effectively bound to FG-COS conjugates through covalent bonds. Additionally, the peak position of the hydrogen bond in FG-COS conjugates and FG–COS–Cur spectra red-shifted from 3334 cm^{-1} to 3346 cm^{-1}, which indicating that the hydrogen bond interaction was also involved in the formation of the complex (Zhang et al., 2021a). Besides, characteristic peaks of Cur were not observed, suggesting that Cur was entrapped inside the FG-COS conjugates. This phenomenon was consistent with Feng et al. (2016).

3.3.4. X-ray diffraction (XRD)

To further confirm the physical state change of Cur after encapsulation in FG-COS conjugates, X-ray diffraction was employed to determine the crystal alterations of Cur. The XRD patterns of Cur, FG-COS conjugates and FG–COS–Cur were illustrated in Fig. 6C. Cur exhibited plenty of sharp peaks in the XRD spectra, indicating that the crystal structure of Cur was highly crystalline. However, FG–COS–Cur nanoparticles were no such sharp peaks, which showed that it could inhibit the formation of Cur crystals, and then formed an amorphous and non-crystalline complex, which was consistent with previous research (Ghobadi et al., 2021).

3.3.5. Evaluation of antioxidant activity of FG–COS–Cur nanoparticles/Cur

Cur was insoluble in water, acidic and neutral buffers, which might cause large errors in experiments. In this experiment, Cur dissolved by absolute ethanol was used as a control (Huang et al., 2016). We fixed the concentration of FG-COS conjugates (1 mg/mL) and investigated the antioxidant capacity of free Cur and FG–COS–Cur nanoparticles at different Cur concentrations. The DPPH free radical scavenging rate of FG–COS–Cur nanoparticles and Cur were compared in Fig. 7A. Cur solubilized in absolute ethanol had poorer scavenging capacity followed by FG–COS–Cur nanoparticles, especially at low concentrations of Cur. The DPPH free radical scavenging rate of FG-COS conjugates (1 mg/mL) was 42.28 ± 0.71%, which showed in Fig. 4A. When the Cur concentration was 8 μg/mL, the DPPH free radical scavenging rate of FG–COS–Cur and Cur were 68.29 ± 1.69% and 24.44 ± 0.93%, respectively. In addition, the FG–COS–Cur nanoparticles had stronger DPPH free radical scavenging rate than the pure Cur at all concentrations, indicating that the nanocompositions with FG-COS conjugates positively influenced the DPPH free radical scavenging rate of free Cur. This was probably because FG-COS shell had excellent antioxidant activity and Cur entered the hydrophobic core of FG-COS conjugates maintained its original antioxidant activity well (O'Toole et al., 2016).

The ABTS free radical scavenging rate of FG–COS–Cur nanoparticles and Cur solubilized in ethanol were also compared in Fig. 7B. The scavenging rate of ABTS free radicals was similar to that of DPPH free radical scavenging activity as we mentioned above. Both the Cur encapsulated in FG-COS conjugates and Cur showed increased scavenging activity on ABTS radicals with the increase of Cur concentrations, but the ABTS radical scavenging of FG–COS–Cur nanoparticles were higher than that of pure Cur. This result suggested that the ABTS free radical scavenging rate of Cur was not affected after the interaction with FG-COS and could be used to form a kind of nanoparticle with higher

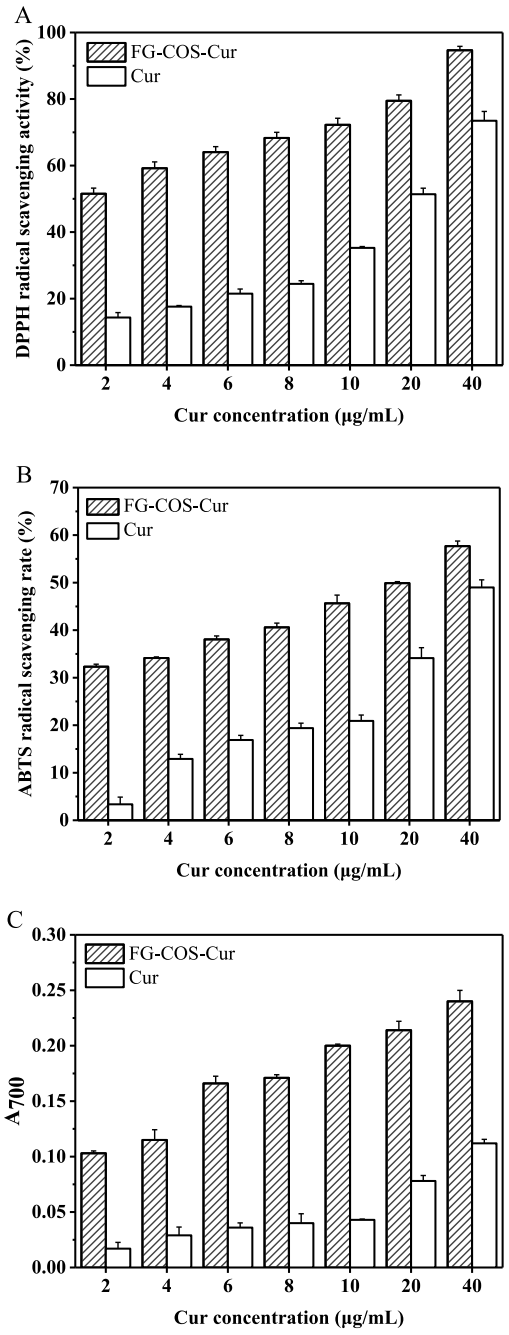

Fig. 7. Antioxidative capacity of FG–COS–Cur and Cur. (A) DPPH radical scavenging rate (B) ABTS radical scavenging rate (C) Reducing power.

ABTS free radical scavenging rate. The ABTS assay findings endorsed our DPPH free radical scavenging activity results.

Research on reducing power was presented in Fig. 7C. As the concentrations of Cur increased, reducing power gradually increased. It was worth noting that Cur had a lower reducing ability, while the FG–COS–Cur nanoparticles had a higher reducing power. FG-COS conjugates manifested amazing reducing power as we mentioned previously (Fig. 4B), after encapsulation of Cur, the reducing power was significantly higher than that of pure Cur. The reducing power of FG-COS conjugates (1 mg/mL) was 0.069 ± 0.003 (data not shown) and the FG–COS–Cur and Cur were 0.214 ± 0.008 and 0.078 ± 0.005, respectively (Cur concentration was 20 μg/mL). This results showed that Cur in nanoparticle form had no negative effect on the antioxidant activity of Cur, instead, FG–COS–Cur exhibited additive reducing power of Cur and FG-COS conjugates. That was in a good accordance with previous researches (Mohammadian et al., 2019).

3.4. Evaluating the antioxidant capacity of FG–COS–Cur on Caco-2 cells

3.4.1. Cytotoxicity and cellular uptake studies of FG–COS–Cur in Caco-2 cells

MTT (Mosmann, 1983) was one of the most used assays for evaluating cytotoxicity. Viability of Caco-2 cells were measured by MTT assay and the results were presented in Fig. 8A–B. The cell studies demonstrated that FG-COS conjugates were almost non-toxic on Caco-2 cells, with cell viability greater than 90% (Fig. 8A). After FG-COS conjugates encapsulated Cur, the cytotoxicity to Caco-2 cell was better than free Cur, especially the concentration of Cur reached 10 μg/mL or 20 μg/mL (Fig. 8B). Besides, cell viability was greater than 80% at all concentrations, which indicated that a good biocompatibility of FG-COS conjugates and Cur with the Caco-2 cell model. According to the above results, several concentrations of Cur (2.5, 5, 10 and 20 μg/mL) were chosen for further experiments.

To study the cellular uptake of FG–COS–Cur nanoparticles and free Cur on Caco-2 cells by measuring the specific fluorescence intensity of Cur in the cells. Both Cur and FG–COS–Cur nanoparticles could be absorbed by Caco-2 cells, which was concentrations-dependent (Fig. 8C). Comparing the intake of Cur and FG-MRP-Cur nanoparticles at the same Cur concentration, it was found that FG–COS–Cur nanoparticles could further enhance the specific fluorescence intensity of Cur, which meant that more Cur was absorbed by Caco-2 cells. When the concentration of Cur increased, the different cellular uptake between FG–COS–Cur nanoparticles and Cur was more obvious, which indicating that FG-COS conjugates could better improve the cellular uptake of Cur by Caco-2 cells. The enhanced uptake behavior of various Cur carrier had been observed previously in many experiments (Song et al., 2018). In short, under the same incubation duration and Cur concentration, Cur in the form of FG–COS–Cur nanoparticles had a better cellular absorption efficiency. This could be owing to Cur's higher solubility after being loaded into the nanostructure.

3.4.2. Establishment of a model of H_2O_2-induced oxidative damage in Caco-2 cells

Oxidative stress referred to a state in which oxidation and antioxidant effects were unbalanced in the body, and ROS were produced and accumulated in large quantities in cells. Excessive productions and accumulations of ROS could destroy intracellular biomolecules. During the experiment, intracellular oxidation of cells could be induced by hydrogen peroxide (Elisia et al., 2008). Thus, H_2O_2 was chosen to induce oxidative stress in Caco-2 cells.

The results of H_2O_2-induced oxidative damage model of Caco-2 cells were displayed in Fig. 9A. Compared with control group, various doses of H_2O_2 had significant effects on the viability of Caco-2 cells ($P < 0.05$) after 4 h of treatment. The cell viability was significantly decreased, indicating that could effectively induce oxidative damage of Caco-2 cells in a concentrations-dependent manner under the different concentrations of H_2O_2 conditions (final concentrations were 100–2000 μM). When the concentration of H_2O_2 in the cell medium was 650 μM, the inhibition rate of Caco-2 cell viability was close to 50%. Therefore, to establish oxidative damage in Caco-2 cells, we choose H_2O_2 final concentration of 650 μM to act on cells for 4 h as the induction condition for subsequent experiments.

3.4.3. Protective effect of FG–COS–Cur/Cur on H_2O_2-induced oxidative damage in Caco-2 cells

The protective effect of FG–COS–Cur nanoparticles and Cur on H_2O_2-induced oxidative damage of Caco-2 cells were measuring in Fig. 9B. Compared with control group, the viability of Caco-2 cells in the positive group (H_2O_2-induced oxidative damage group) was significantly reduced, which was about 60%. With the increase of Cur concentrations,

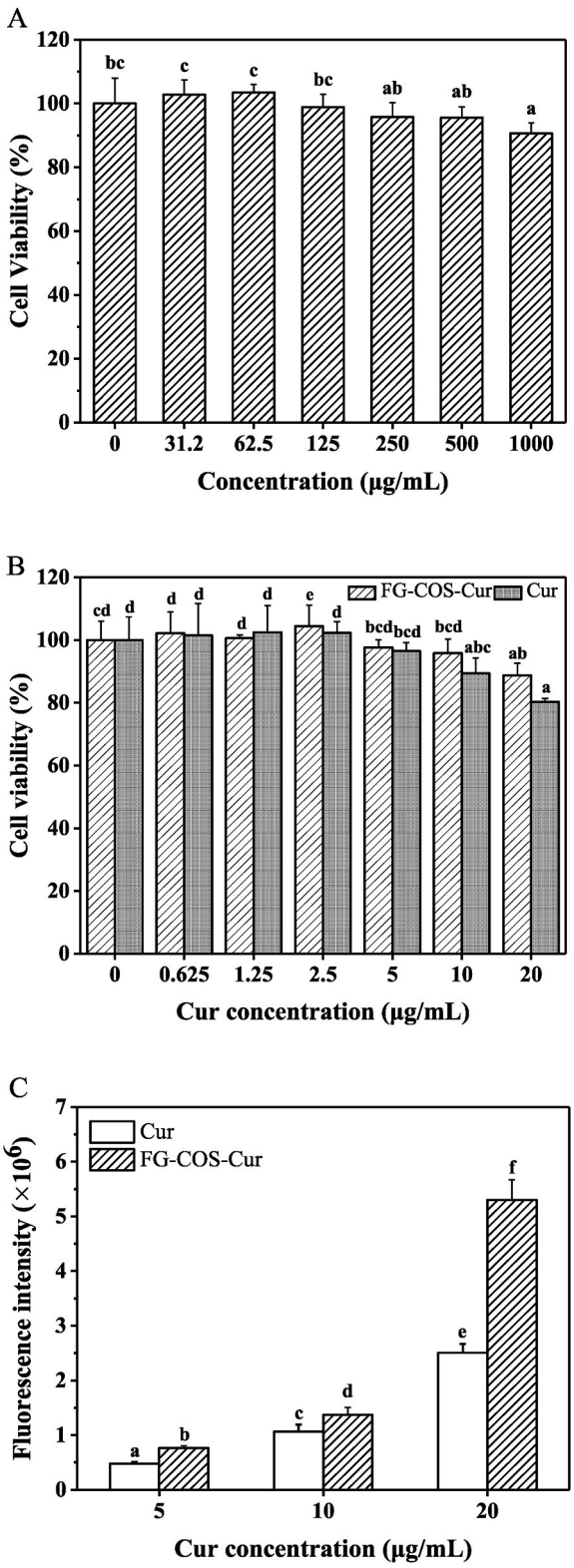

Fig. 8. The effect of FG–COS–Cur nanoparticles and Cur on Caco-2 cells. Different lowercase letters represented as significant difference at $P < 0.05$. (A) Cell viability after treatment with FG-COS conjugates. (B) Cell viability after treatment with FG–COS–Cur and Cur. (C) Cellular uptake of FG–COS–Cur and Cur.

the viability of Caco-2 cells in the sample protection group increased significantly when treated with different concentrations of FG–COS–Cur nanoparticles and Cur (5, 10, 20 μg/mL of Cur). Notably, when the concentration of Cur was 20 μg/mL, the viability of Caco-2 cells rose by 24% and 11%, respectively, when compared to the positive group. Moreover, the effect of FG-MRP-Cur nanoparticles were significantly higher than that of pure Cur, especially at high concentrations. This might be due to the shell of FG–COS–Cur nanoparticles possessed efficient encapsulation to improve solubility and outstanding antioxidation to superimpose antioxidant ability as we previously mentioned. Thus, a pretreatment with FG–COS–Cur nanoparticles and Cur inhibited cell death, indicating the ability of decreasing intracellular oxidation (Samaranayaka et al., 2011).

3.4.4. Effects of FG–COS–Cur on ROS levels in Caco-2 cells induced by H_2O_2

ROS influenced numerous biological functions, including cell growth, adhesion, and apoptosis (Hossen et al., 2020). However, too much ROS could disturb normal physiological processes by affecting the concentrations of many enzymes and other associated molecules in the gut (Piechota-Polanczyk et al., 2014). Thus, we determined the effect of FG–COS–Cur nanoparticles on ROS levels in Caco-2 cells induced by H_2O_2 (Fig. 9C). As shown, H_2O_2 treatment significantly increased the intracellular ROS level in Caco-2 cells, while the intracellular ROS level was significantly reduced and presented a dose relationship after treatment with different concentrations of FG–COS–Cur nanoparticles. When the concentration of Cur was 20 μg/mL, the intracellular ROS level of Caco-2 decreased to the lowest level, and exhibited no statistically significant change as compared to the control group. The reduction of ROS levels employing FG–COS–Cur nanoparticles, accompanied by the high DPPH and ABTS radical scavenging capacity and the reducing power (Fig. 7A–C), suggested that free radical sequestration or neutralization was a plausible mechanism of action in the FG–COS–Cur nanoparticles (Gomez et al., 2019). The above results revealed that FG–COS–Cur nanoparticles could effectively reduce the ROS level of Caco-2 cells induced by H_2O_2, thereby alleviating oxidative damage and protecting cells.

3.4.5. Effects of FG–COS–Cur on extracellular lactate dehydrogenase levels in Caco-2 cells induced by H_2O_2

LDH was an important indicator of cell membrane integrity (He et al., 2018). During the process of oxidative damage, cells would release intracellular LDH into the culture medium, so the activity of LDH in the culture supernatant could reflect the degree of cell damage. To determine the effect of FG–COS–Cur nanoparticles treatment on H_2O_2-induced Caco-2 cells further, we checked the LDH level (Fig. 9D). This results showed that in the positive group of H_2O_2-induced oxidative damage, LDH was significantly increased, indicating that H_2O_2-induced oxidative damage to the cell membrane structure, resulting in weakened antioxidant function. Compared with positive group, the LDH level of the FG–COS–Cur nanoparticles treatment group was significantly decreased, indicating that FG–COS–Cur nanoparticles had obvious antioxidant biological activity. This dose-dependent decreased might be attributable to the scavenging of exogenous free radicals in cells by the FG–COS–Cur nanoparticles, which reduced LDH level increasing (Fan et al., 2013).

3.4.6. Effects of FG–COS–Cur on intracellular antioxidant enzyme activities in Caco-2 cells induced by H_2O_2

These preliminary findings motivated us to investigate the antioxidant properties of FG–COS–Cur nanoparticles at the cellular level further. To understand the antioxidative effect of FG–COS–Cur nanoparticles further, we evaluated the activity of intracellular antioxidant enzymes in FG–COS–Cur nanoparticles treated cells under oxidative stress. FG–COS–Cur groups exhibited significantly increased SOD (Fig. 9E) and CAT (Fig. 9F) enzyme activity compared with both positive

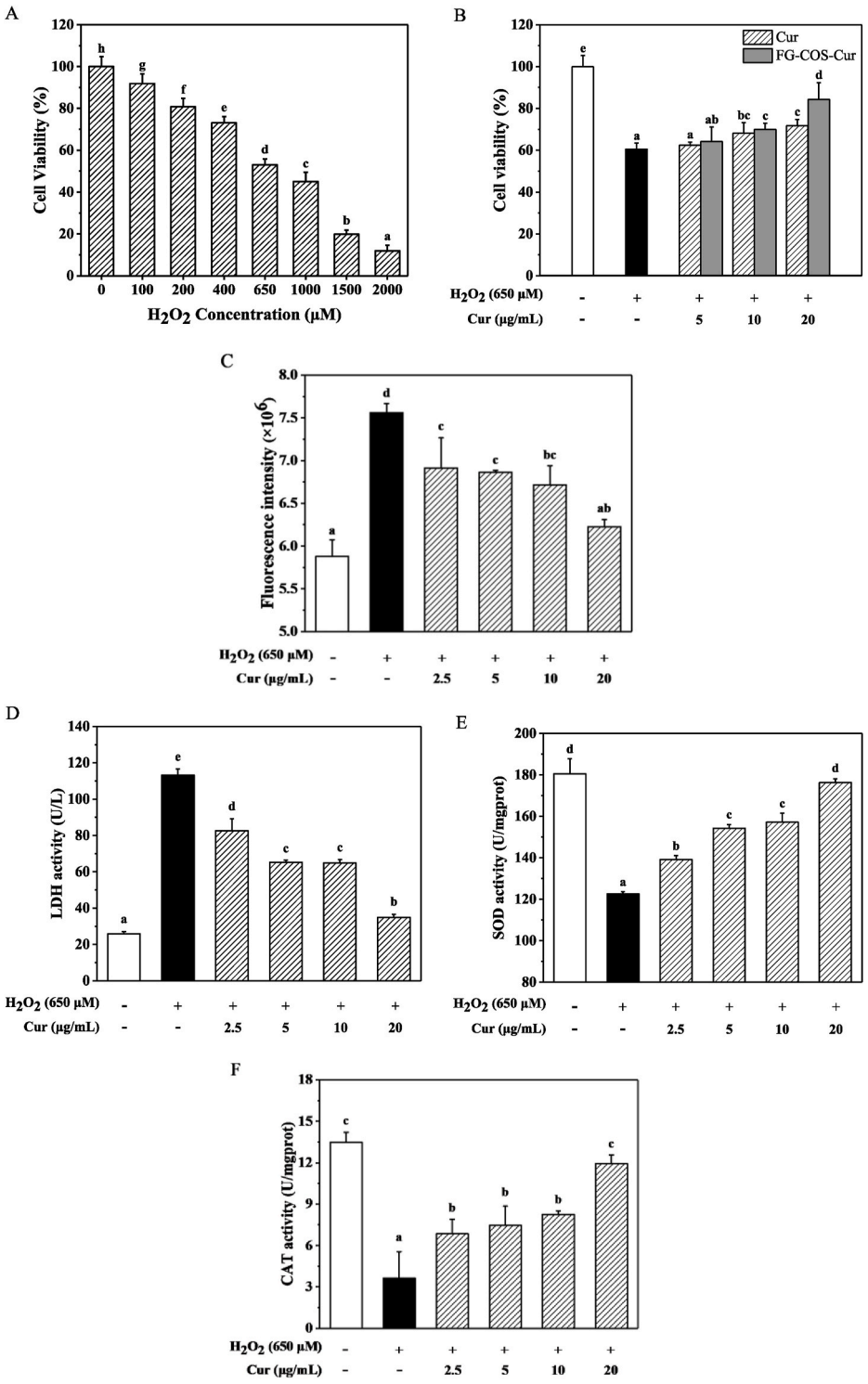

Fig. 9. Study of FG–COS–Cur nanoparticles on H_2O_2-induced oxidative damage of Caco-2 cells. Different lowercase letters represented as significant difference at $P < 0.05$. (A) Effect of different concentrations of H_2O_2 on the viability of Caco-2 cells. (B) Protective effect of FG–COS–Cur and Cur on H_2O_2-induced oxidative damage in Caco-2 cells. (C) Effect of FG–COS–Cur on ROS levels in Caco-2 cells induced by H_2O_2. (D) Effect of FG–COS–Cur on LDH levels in Caco-2 cells induced by H_2O_2. (E) Effect of FG–COS–Cur on SOD levels in Caco-2 cells induced by H_2O_2. (F) Effect of FG–COS–Cur on CAT levels in Caco-2 cells induced by H_2O_2.

control groups ($P < 0.05$), which exhibited a dose-response relationship in the range of measured concentrations. In addition, the low- and middle-dose groups exhibited significantly higher SOD and CAT enzyme activity levels than the positive control group ($P < 0.05$), which exhibited excellent antioxidant capacity to reduce H_2O_2-induced oxidative damage in Caco-2 cells. In this study, FG–COS–Cur nanoparticles had a protective effect on H_2O_2-induced oxidative damage in Caco-2 cells, which might be related to the enhanced antioxidant capacity of Cur loaded in FG-COS conjugates.

4. Conclusions

In summary, a funtional carrier (FG-COS conjugates) was easily fabricated via the Maillard reaction and utilized to improve the stability, antioxidation and bioavailability of Cur. The FG-COS conjugates could significantly improve surface hydrophobicity and possess superb antioxidant capacity than FG. Further, Cur was encapsulated by FG-COS conjugates with high encapsulation efficiency and good UV stability. The fluorescence spectrometry, FTIR and XRD indicated that the Cur was embedded. The DPPH, ABTS radical scavenging ability and

reducing power of FG–COS–Cur nanoparticles showing a superimposed antioxidant capacity between Cur and FG-COS conjugates. Cur, a poorly absorbed hydrophobic bioactive molecule, had a considerable increased in cellular absorption efficiency after being loaded into FG-COS conjugates. FG–COS–Cur nanoparticles well protected H_2O_2-induced oxidative damage in Caco-2 cells by reducing ROS generation, LDH enzyme activity and increasing SOD, CAT enzyme activity, possessing significant difference with control at lower Cur concentrations. It could be concluded that the encapsulation of Cur in FG-COS conjugates was a promising approach to improve the antioxidation and bioavailability for Cur and had the potential to become a nano-delivery system for small molecule active substances.

CRediT authorship contribution statement

Sheng Lin: Methodology, Software, Validation, Investigation, Writing – original draft. **Xixi Cai:** Methodology, Investigation. **Huimin Chen:** Resources, Writing – review & editing. **Yizhou Xu:** Methodology, Investigation. **Jiulin Wu:** Formal analysis, Visualization, Data curation, Writing – review & editing, Project administration. **Shaoyun Wang:** Conceptualization, Supervision, Funding acquisition.

Declaration of competing interest

The authors declare that they have no known competing financial interests or personal relationships that could have appeared to influence the work reported in this paper.

Acknowledgements

This work was supported by National Natural Science Foundation of China (32272311); Fujian Major Project of Provincial Science & Technology Hall (2020NZ010008), China; Central government guided local science and technology development projects (2020L3004), China.

Appendix A. Supplementary data

Supplementary data to this article can be found online at https://doi.org/10.1016/j.crfs.2022.09.019.

References

Ajandouz, E.H., Tchiakpe, L.S., Ore, F.D., Benajiba, A., Puigserver, A., 2001. Effects of pH on caramelization and maillard reaction kinetics in fructose-lysine model systems. J. Food Sci. 66, 926–931.
Bao, C., Jiang, P., Chai, J., Jiang, Y., Li, D., Bao, W., Liu, B., Liu, B., Norde, W., Li, Y., 2019. The delivery of sensitive food bioactive ingredients: absorption mechanisms, influencing factors, encapsulation techniques and evaluation models. Food Res. Int. 120, 130–140.
Belatik, A., Hotchandani, S., Bariyanga, J., Tajmir-Riahi, H.A., 2012. Binding sites of retinol and retinoic acid with serum albumins. Eur. J. Med. Chem. 48, 114–123.
Benjakul, S., Lertittikul, W., Bauer, F., 2005. Antioxidant activity of Maillard reaction products from a porcine plasma protein-sugar model system. Food Chem. 93, 189–196.
Bernardo, A., Plumitallo, C., De Nuccio, C., Visentin, S., Minghetti, L., 2021. Curcumin promotes oligodendrocyte differentiation and their protection against TNF-alpha through the activation of the nuclear receptor PPAR-gamma. Sci. Rep. 11, 4952.
Bourbon, A.I., Cerqueira, M.A., Vicente, A.A., 2016. Encapsulation and controlled release of bioactive compounds in lactoferrin-glycomacropeptide nanohydrogels: curcumin and caffeine as model compounds. J. Food Eng. 180, 110–119.
Cai, X., Weng, Q., Lin, J., Chen, G., Wang, S., 2021. Radix Pseudostellariae protein-curcumin nanocomplex: improvement on the stability, cellular uptake and antioxidant activity of curcumin. Food Chem. Toxicol. 151, 112110.
Cao, R., Zhao, Y., Zhou, Z., Zhao, X., 2018. Enhancement of the water solubility and antioxidant activity of hesperidin by chitooligosaccharide. J. Sci. Food Agric. 98, 2422–2427.
Chen, W., Lv, R., Wang, W., Ma, X., Muhammad, A.I., Guo, M., Ye, X., Liu, D., 2019a. Time effect on structural and functional properties of whey protein isolate-gum acacia conjugates prepared via Maillard reaction. J. Sci. Food Agric. 99, 4801–4807.
Chen, W., Wang, W., Ma, X., Lv, R., Watharkar, R.B., Ding, T., Ye, X., Liu, D., 2019b. Effect of pH-shifting treatment on structural and functional properties of whey protein isolate and its interaction with (-)-epigallocatechin-3-gallate. Food Chem. 274, 234–241.
Cheng, C., Peng, S., Li, Z., Zou, L., Liu, W., Liu, C., 2017. Improved bioavailability of curcumin in liposomes prepared using a pH-driven, organic solvent-free, easily scalable process. RSC Adv. 7, 25978–25986.
Chung, C., Rojanasasithara, T., Mutilangi, W., McClements, D.J., 2016. Enhancement of colour stability of anthocyanins in model beverages by gum Arabic addition. Food Chem. 201, 14–22.
Dai, C., Zhang, W., He, R., Xiong, F., Ma, H., 2017. Protein breakdown and release of antioxidant peptides during simulated gastrointestinal digestion and the absorption by everted intestinal sac of rapeseed proteins. LWT–Food Sci. Technol. 86, 424–429.
Dezhampanah, H., Shabanzade, Z., 2022. Investigation of binding interaction between human serum albumin with zirconium complex of curcumin and curcumin. J. Biomol. Struct. Dyn. 40, 722–732.
Elisia, I., Kitts, D.D., 2008. Anthocyanins inhibit peroxyl radical-induced apoptosis in Caco-2 cells. Mol. Cell. Biochem. 312, 139–145.
Eric, K., Raymond, L.V., Huang, M., Cheserek, M.J., Hayat, K., Savio, N.D., Amédée, M., Zhang, X., 2013. Sensory attributes and antioxidant capacity of Maillard reaction products derived from xylose, cysteine and sunflower protein hydrolysate model system. Food Res. Int. 54, 1437–1447.
Fan, J.P., Fan, C., Dong, W.M., Gao, B., Yuan, W., Gong, J.S., 2013. Free radical scavenging and anti-oxidative activities of an ethanol-soluble pigment extract prepared from fermented Zijuan Pu-erh tea. Food Chem. Toxicol. 59, 527–533.
Fan, Y., Yi, J., Zhang, Y., Yokoyama, W., 2018. Fabrication of curcumin-loaded bovine serum albumin (BSA)-dextran nanoparticles and the cellular antioxidant activity. Food Chem. 239, 1210–1218.
Feng, J., Wu, S., Wang, H., Liu, S., 2016. Improved bioavailability of curcumin in ovalbumin-dextran nanogels prepared by Maillard reaction. J. Funct.Foods 27, 55–68.
Gharbi, N., Labbafi, M., 2019. Influence of treatment-induced modification of egg white proteins on foaming properties. Food Hydrocolloids 90, 72–81.
Ghobadi, M., Koocheki, A., Varidi, M.J., Varidi, M., 2021. Encapsulation of curcumin using Grass pea (Lathyrus sativus) protein isolate/Alyssum homolocarpum seed gum complex nanoparticles. Innov. Food Sci. Emerg. 72, 102728.
Gomez, L.J., Gomez, N.A., Zapata, J.E., Lopez-Garcia, G., Cilla, A., Alegria, A., 2019. In-vitro antioxidant capacity and cytoprotective/cytotoxic effects upon Caco-2 cells of red tilapia (Oreochromis spp.) viscera hydrolysates. Food Res. Int. 120, 52–61.
Guerrero, P., Garrido, T., Leceta, I., de la Caba, K., 2013. Films based on proteins and polysaccharides: preparation and physical-chemical characterization. Eur. Polym. J. 49, 3713–3721.
Han, M.M., Yi, Y., Wang, H.X., Huang, F., 2017. Investigation of the maillard reaction between polysaccharides and proteins from longan pulp and the improvement in activities. Molecules 22 (6), 938.
Haskard, C.A., Li-Chan, E.C.Y., 1998. Hydrophobicity of bovine serum albumin and ovalbumin determined using uncharged (PRODAN) and anionic (ANS(-)) fluorescent probes. J. Agric. Food Chem. 46, 2671–2677.
He, N., Tian, L., Zhai, X., Zhang, X., Zhao, Y., 2018. Composition characterization, antioxidant capacities and anti-proliferative effects of the polysaccharides isolated from Trametes lactinea (Berk.) Pat. Int. J. Biol. Macromol. 115, 114–123.
Hossen, I., Hua, W., Ting, L., Mehmood, A., Jingyi, S., Duoxia, X., Yanping, C., Hongqing, W., Zhipeng, G., Kaiqi, Z., Fang, Y., Junsong, X., 2020. Phytochemicals and inflammatory bowel disease: a review. Crit. Rev. Food Sci. Nutr. 60, 1321–1345.
Hu, Z.Z., Sha, X.M., Huang, T., Yuan, C.H., Chen, W.M., Li, X.X., Tu, Z.C., 2021. Gelling properties and structure modification of tilapia skin gelatin by the addition of γ-polyglutamic acid at different pH levels. Int. J. Food Sci. Technol. 56, 5812–5823.
Huang, T., Tu, Z., Zou, Z., Shangguan, X., Wang, H., Bansal, N., 2020. Glycosylated fish gelatin emulsion: rheological, tribological properties and its application as model coffee creamers. Food Hydrocolloids 102, 105552.
Huang, X., Huang, X., Gong, Y., Xiao, H., McClements, D.J., Hu, K., 2016. Enhancement of curcumin water dispersibility and antioxidant activity using core-shell protein-polysaccharide nanoparticles. Food Res. Int. 87, 1–9.
Jia, C., Cao, D., Ji, S., Lin, W., Zhang, X., Muhoza, B., 2020. Whey protein isolate conjugated with xylo-oligosaccharides via maillard reaction: characterization, antioxidant capacity, and application for lycopene microencapsulation. LWT–Food Sci. Technol. 118, 108837.
Jiang, T., Liao, W., Charcosset, C., 2020. Recent advances in encapsulation of curcumin in nanoemulsions: a review of encapsulation technologies, bioaccessibility and applications. Food Res. Int. 132, 109035.
Jordan, B.C., Mock, C.D., Thilagavathi, R., Selvam, C., 2016. Molecular mechanisms of curcumin and its semisynthetic analogues in prostate cancer prevention and treatment. Life Sci. 152, 135–144.
Kchaou, H., Benbettaieb, N., Jridi, M., Nasri, M., Debeaufort, F., 2019. Influence of Maillard reaction and temperature on functional, structure and bioactive properties of fish gelatin films. Food Hydrocolloids 97, 105196.
Kim, S., Rajapakse, N., 2005. Enzymatic production and biological activities of chitosan oligosaccharides (COS): a review. Carbohydr. Polym. 62, 357–368.
Li, Z., Lin, Q., McClements, D.J., Fu, Y., Xie, H., Li, T., Chen, G., 2021. Curcumin-loaded core-shell biopolymer nanoparticles produced by the pH-driven method: physicochemical and release properties. Food Chem. 355, 129686.
Liang, R., Cheng, S., Dong, Y., Ju, H., 2019. Intracellular antioxidant activity and apoptosis inhibition capacity of PEF-treated KDHCH in HepG2 cells. Food Res. Int. 121, 336–347.
Liu, Y., Cai, Y., Ying, D., Fu, Y., Xiong, Y., Le, X., 2018. Ovalbumin as a carrier to significantly enhance the aqueous solubility and photostability of curcumin: interaction and binding mechanism study. Int. J. Biol. Macromol. 116, 893–900.
Luo, Y., Ling, Y., Wang, X., Han, Y., Zeng, X., Sun, R., 2013. Maillard reaction products from chitosan-xylan ionic liquid solution. Carbohydr. Polym. 98, 835–841.

Lv, L.-C., Huang, Q.-Y., Ding, W., Xiao, X.-H., Zhang, H.-Y., Xiong, L.-X., 2019. Fish gelatin: the novel potential applications. J. Funct.Foods 63, 103581.
Mohammadian, M., Salami, M., Moghadam, M., Amirsalehi, A., Emam-Djomeh, Z., 2021. Mung bean protein as a promising biopolymeric vehicle for loading of curcumin: structural characterization, antioxidant properties, and in vitro release kinetics. J. Drug Deliv. Sci. Technol. 61, 102148.
Mohammadian, M., Salami, M., Momen, S., Alavi, F., Emam-Djomeh, Z., 2019. Fabrication of curcumin-loaded whey protein microgels: structural properties, antioxidant activity, and in vitro release behavior. LWT–Food Sci. Technol. 103, 94–100.
Mosmann, T., 1983. Rapid colorimetric assay for cellular growth and survival: application to proliferation and cytotoxicity assays. J. Immunol. Methods 65, 55–63.
O'Toole, M.G., Soucy, P.A., Chauhan, R., Raju, M.V., Patel, D.N., Nunn, B.M., Keynton, M.A., Ehringer, W.D., Nantz, M.H., Keynton, R.S., Gobin, A.S., 2016. Release-modulated antioxidant activity of a composite curcumin-chitosan polymer. Biomacromolecules 17, 1253–1260.
Oliver, C.M., Kher, A., McNaughton, D., Augustin, M.A., 2009. Use of FTIR and mass spectrometry for characterization of glycated caseins. J. Dairy Res. 76, 105–110.
Piechota-Polanczyk, A., Fichna, J., 2014. Review article: the role of oxidative stress in pathogenesis and treatment of inflammatory bowel diseases. N-S Arch. Pharmacol. 387, 605–620.
Pirestani, S., Nasirpour, A., Keramat, J., Desobry, S., Jasniewski, J., 2018. Structural properties of canola protein isolate-gum Arabic Maillard conjugate in an aqueous model system. Food Hydrocolloids 79, 228–234.
Rauf, A., Imran, M., Orhan, I.E., Bawazeer, S., 2018. Health perspectives of a bioactive compound curcumin: a review. Trends Food Sci. Technol. 74, 33–45.
Samaranayaka, A.G.P., Li-Chan, E.C.Y., 2011. Food-derived peptidic antioxidants: a review of their production, assessment, and potential applications. J. Funct. Foods 3, 229–254.
Sheng, L., Tang, G., Wang, Q., Zou, J., Ma, M., Huang, X., 2020. Molecular characteristics and foaming properties of ovalbumin-pullulan conjugates through the Maillard reaction. Food Hydrocolloids 100, 105384.
Shi, Y., Liang, R., Chen, L., Liu, H., Goff, H.D., Ma, J., Zhong, F., 2019. The antioxidant mechanism of Maillard reaction products in oil-in-water emulsion system. Food Hydrocolloids 87, 582–592.
Song, W., Su, X., Gregory, D.A., Li, W., Cai, Z., Zhao, X., 2018. Magnetic alginate/chitosan nanoparticles for targeted delivery of curcumin into human breast cancer cells. Nanomaterials 8, 907.
Sow, L.C., Toh, N.Z.Y., Wong, C.W., Yang, H., 2019. Combination of sodium alginate with tilapia fish gelatin for improved texture properties and nanostructure modification. Food Hydrocolloids 94, 459–467.
Spotti, M.J., Loyeau, P.A., Marangón, A., Noir, H., Rubiolo, A.C., Carrara, C.R., 2019. Influence of Maillard reaction extent on acid induced gels of whey proteins and dextrans. Food Hydrocolloids 91, 224–231.
Stanciuc, N., Aprodu, I., Ionita, E., Bahrim, G., Rapeanu, G., 2015. Exploring the process-structure-function relationship of horseradish peroxidase through investigation of pH- and heat induced conformational changes. Spectrochim. Acta Mol. Biomol. Spectrosc. 147, 43–50.
Su, J.-F., Huang, Z., Yuan, X.-Y., Wang, X.-Y., Li, M., 2010. Structure and properties of carboxymethyl cellulose/soy protein isolate blend edible films crosslinked by Maillard reactions. Carbohydr. Polym. 79, 145–153.
Sun, X., Cui, Q., Li, R., Hao, L., Liu, H., Wang, X., Xu, N., Zhao, X., 2022. Structural and emulsifying properties of soybean protein isolate glycated with glucose based on pH treatment. J. Sci. Food Agric. 102 (11), 4462–4472.
Wang, B., Li, Z.R., Chi, C.F., Zhang, Q.H., Luo, H.Y., 2012. Preparation and evaluation of antioxidant peptides from ethanol-soluble proteins hydrolysate of Sphyrna lewini muscle. Peptides 36, 240–250.
Wang, L., Gulati, P., Santra, D., Rose, D., Zhang, Y., 2018. Nanoparticles prepared by proso millet protein as novel curcumin delivery system. Food Chem. 240, 1039–1046.
Wang, L., Xiao, M., Dai, S., Song, J., Ni, X., Fang, Y., Corke, H., Jiang, F., 2014. Interactions between carboxymethyl konjac glucomannan and soy protein isolate in blended films. Carbohydr. Polym. 101, 136–145.
Wang, Z., Liu, H., Liu, Q., Chen, Q., Kong, B., 2021. A literature review of the application of maillard reaction and its products in the delivery of bioactive substances. Food Sci. (N. Y.) 42, 324–331.
Weng, Q., Cai, X., Zhang, F., Wang, S., 2019. Fabrication of self-assembled Radix Pseudostellariae protein nanoparticles and the entrapment of curcumin. Food Chem. 274, 796–802.
Wu, J., Sun, X., Guo, X., Ji, M., Wang, J., Cheng, C., Chen, L., Wen, C., Zhang, Q., 2017. Physicochemical, antioxidant, in vitro release, and heat sealing properties of fish gelatin films incorporated with β-cyclodextrin/curcumin complexes for apple juice preservation. Food Bioprocess Technol. 11, 447–461.
Wu, S., Dai, X., Shilong, F., Zhu, M., Shen, X., Zhang, K., Li, S., 2018. Antimicrobial and antioxidant capacity of glucosamine-zinc(II) complex via non-enzymatic browning reaction. Food Sci. Biotechnol. 27, 1–7.
Yan, F., Yu, X., Jing, Y., 2018. Optimized preparation, characterization, and antioxidant activity of chitooligosaccharide-glycine Maillard reaction products. J. Food Sci. Technol. 55, 712–720.
Yang, H., Wen, X.L., Guo, S.G., Chen, M.T., Jiang, A.M., Lai, L.-S., 2015. Physical, antioxidant and structural characterization of blend films based on hsian-tsao gum (HG) and casein (CAS). Carbohydr. Polym. 134, 222–229.
Yang, R., Hui, Q., Jiang, Q., Liu, S., Zhang, H., Wu, J., Lin, F., O, K., Yang, C., 2019. Effect of manitoba-grown red-osier dogwood extracts on recovering caco-2 cells from H2O2-induced oxidative damage. Antioxidants 8, 250.
Yi, J., Peng, G., Zheng, S., Wen, Z., Gan, C., Fan, Y., 2021. Fabrication of whey protein isolate-sodium alginate nanocomplex for curcumin solubilization and stabilization in a model fat-free beverage. Food Chem. 348, 129102.
Yoshimura, Y., Iijima, T., Watanabe, T., Nakazawa, H., 1997. Antioxidative effect of Maillard reaction products using glucose-glycine model system. J. Agric. Food Chem. 45, 4106–4109.
Yu, X., Jing, Y., Yan, F., 2019. Chitooligosaccharide–lysine maillard reaction products: preparation and potential application on fresh-cut kiwifruit. ood Bioprocess Tech 12, 1133–1143.
Yuan, X., Zheng, J., Jiao, S., Cheng, G., Feng, C., Du, Y., Liu, H., 2019. A review on the preparation of chitosan oligosaccharides and application to human health, animal husbandry and agricultural production. Carbohydr. Polym. 220, 60–70.
Yue, Y., Zhang, Y., Zhou, L., Qin, J., Chen, X., 2008. In vitro study on the binding of herbicide glyphosate to human serum albumin by optical spectroscopy and molecular modeling. J. Photochem. Photobiol., B 90, 26–32.
Zhang, B., Chi, Y.J., Li, B., 2013. Effect of ultrasound treatment on the wet heating Maillard reaction between β-conglycinin and maltodextrin and on the emulsifying properties of conjugates. Eur. Food Res. Technol. 238, 129–138.
Zhang, D., Jiang, F., Ling, J., Ouyang, X.K., Wang, Y.G., 2021a. Delivery of curcumin using a zein-xanthan gum nanocomplex: fabrication, characterization, and in vitro release properties. Colloids Surf., B 204, 111827.
Zhang, X., Li, Y., Guo, M., Jin, T.Z., Arabi, S.A., He, Q., Ismail, B.B., Hu, Y., Liu, D., 2021b. Antimicrobial and UV blocking properties of composite chitosan films with curcumin grafted cellulose nanofiber. Food Hydrocolloids 112, 106337.
Zhang, X., Wei, Z., Wang, X., Wang, Y., Tang, Q., Huang, Q., Xue, C., 2022. Fabrication and characterization of core-shell gliadin/tremella polysaccharide nanoparticles for curcumin delivery: encapsulation efficiency, physicochemical stability and bioaccessibility. Curr. Res. Food Sci. 5, 288–297.
Zhang, Z., Wang, X., Yu, J., Chen, S., Ge, H., Jiang, L., 2017. Freeze-thaw stability of oil-in-water emulsions stabilized by soy protein isolate-dextran conjugates. LWT–Food Sci. Technol. 78, 241–249.
Zhong, L., Ma, N., Wu, Y., Zhao, L., Ma, G., Pei, F., Hu, Q., 2019. Characterization and functional evaluation of oat protein isolate-Pleurotus ostreatus β-glucan conjugates formed via Maillard reaction. Food Hydrocolloids 87, 459–469.
Zhu, D., Damodaran, S., Lucey, J.A., 2010. Physicochemical and emulsifying properties of whey protein isolate (WPI)-dextran conjugates produced in aqueous solution. J. Agric. Food Chem. 58, 2988–2994.
Zhu, J., Sun, X., Wang, S., Xu, Y., Wang, D., 2017. Formation of nanocomplexes comprising whey proteins and fucoxanthin: characterization, spectroscopic analysis, and molecular docking. Food Hydrocolloids 63, 391–403.